Hafnia-basierte Nanopartikel zur Bildgebung und Therapie mit biologischen Entitäten

Anpassung der physikalisch-chemischen Eigenschaften und Wechselwirkungen

DIPLOMARBEIT

zur Erlangung des akademischen Grades

Diplom-Ingenieur

im Rahmen des Studiums

Biomedical Engineering

eingereicht von

Lukas Gerken

Ludwigstr. 5, 88131 Lindau, Germany

Matrikelnummer 1527948

unter der Anleitung von

Univ.Prof. Dipl.-Ing. Dr. Peter Ertl, Institut für Angewandte Synthesechemie, TUW, Wien
Dr. Inge Katrin Herrmann, Groupleader Particles 4D, EMPA, St. Gallen

an der Fakultät für Technische Chemie

der Technischen Universität Wien

Wien, 3. Oktober 2017

_____

Lukas Gerken

Hafnia-based Nanoparticles for Imaging and Therapy

Tailoring the Physicochemical Properties and Interactions with Biological Entities

DIPLOMA THESIS

submitted in partial fulfillment of the requirements for the degree of

Diplom-Ingenieur

in

Biomedical Engineering

by

Lukas Gerken

Ludwigstr. 5, 88131 Lindau, Germany

Registration Number 1527948

under supervision of

Univ.Prof. Dipl.-Ing. Dr. Peter Ertl, Institut für Angewandte Synthesechemie, TUW, Wien

Dr. Inge Katrin Herrmann, Groupleader Particles 4D, EMPA, St. Gallen

to the Faculty of Technical Chemistry

at the TU Wien

Vienna, 3rd October, 2017

_____

Lukas Gerken

Erklärung zur Verfassung der Arbeit

Lukas Gerken
Ludwigstr. 5, 88131 Lindau, Germany

Hiermit erkläre ich, dass ich diese Arbeit selbständig verfasst habe, dass ich die verwendeten Quellen und Hilfsmittel vollständig angegeben habe und dass ich die Stellen der Arbeit – einschließlich Tabellen, Karten und Abbildungen –, die anderen Werken oder dem Internet im Wortlaut oder dem Sinn nach entnommen sind, auf jeden Fall unter Angabe der Quelle als Entlehnung kenntlich gemacht habe.

Wien, 3. Oktober 2017

_____
Lukas Gerken

Danksagung

Gerne bedanke ich mich bei der EMPA für die Gelegenheit professionell und individuell zu lernen und der TUW für die Zusammenarbeit, die eine externe These möglich gemacht hat. Speziell möchte ich mich bei Dr. Inge Katrin Herrmann (EMPA) und bei Prof. Peter Ertl (TUW) für eine fantastische Betreuung bedanken. Darüber hinaus danke ich Yucheng Zhang (EMPA) für die Hilfe bei TEM-Bildern, dem 'Center for X-Ray Analytics' (EMPA) für die Rötgendiffraktometrischen Aufnahmen, Adrian Wichser (EMPA) für Elementanalysen und Inge's Team für die Bereitschaft, jederzeit zu helfen.

Acknowledgements

I would like to thank EMPA for the opportunity to learn, professionally and individually, and TUW for the collaboration making an external thesis possible. Special thanks go to Dr. Inge Katrin Herrmann (EMPA) and Prof. Peter Ertl (TUW) for fantastic supervision. Furthermore I thank Yucheng Zhang (EMPA) for helping with acquiring TEM images, the Center for X-Ray Analytics (EMPA) for taking powder diffraction patterns, Adrian Wichser (EMPA) for elemental analysis and Inge's team for their willingness to help at any time.

Kurzfassung

Krebs-Therapie bleibt ein wichtiges globales Thema. Während Behandlungsmodalitäten wie chirurgische Resektion, Chemotherapie, Strahlentherapie und thermische Ablation das Überleben des Patienten erhöht haben, verringert die im Verlauf der Therapie erworbene Resistenz den gesamten therapeutischen Erfolg. Um die Behandlungswirksamkeit zu maximieren und die Nebenwirkungen zu minimieren, ist die Zellselektivität ein wichtiges Ziel. Die Therapie sollte exklusiv an die Tumorzellen mit minimaler Wirkung auf gesundes Gewebe abgegeben werden. Es wurden verschiedene Ansätze entwickelt, um Strahlungsresistenzien zu verringern und gleichzeitig die Wirksamkeit und Sicherheit der Strahlentherapie zu verbessern.

Nanopartikel (NPs) sind als Bildgebungssonden vielversprechend und als Radiosensibilisatoren, um die Spezifität zu erhöhen. Trotz zahlloser Anregungen in der wissenschaftlichen Gemeinschaft weist die Translation von Nanopartikel-basierten Konzepten erhebliche Lücken auf, insbesondere im Bereich der Biomedizin [23]. Unter den kommerziell erhältlichen Nanomedizin Produkten ist die Mehrheit Liposomal-basiert. Andere vermarktete Produkte umfassen polymere Nanostrukturen und Eisenoxid-Nanopartikel [16, 30, 44].

Unter der Fülle von Nanomaterialien mit nutzbaren Eigenschaften hat Hafniumdioxid aufgrund der hohen Dielektrizitätskonstante ($\epsilon = 25$), dem hohen Schmelzpunkt (2758 °C), einer hohen Ordnungszahl ($Z = 72$), hohen Dichte (9,7 g cm^{-3}), hohen Brechungsindex, transparenz zu sichtbarem Licht (5,3-5,9 eV Bandlücke) und chemische Inertheit. Ein HfO2-Nanopartikel-basiertes Produkt (NBTXR3, Nanobiotix), zu Nutzung als Radiosensibilisator, wurde vor kurzem zur Marktzulassung vorgelegt [44]. Allerdings ist das Verständnis über die Materialeigenschaften und insbesondere über das Potenzial von Hafnia als Matrix für multimodale theranosti-

sche biologische Bildgebung und damit die Kombination von Röntgenbildgebung mit Radiosensibilisierung, mit Lanthanoid-dotierter Lumineszenz und mit MRT-Bildgebung, bisher weitgehend eingeschränkt.

Diese Masterarbeit ist auf jene Lücke gerichtet und untersucht die Materialeigenschaften und die anwendungsbezogenen Eigenschaften von Hafnia-basierten Nanopartikeln für biomedizinische Anwendungen. Undotierte und Lanthanoid-dotierte HfO_2 NPs wurden mit verschiedenen Methoden synthetisiert und anschließend mit PVP, APTES und Folsäure funktionalisiert. Partikelgröße, Form und Morphologie wurden durch Elektronenmikroskopie bestimmt. Struktur und Kristallinität wurde anhand von Röntgenbeugung gemessen. Photolumineszens Intensitäten und Lebensdauern wurden für Eu^{3+} und Tb^{3+} dotierte NPs in zwei verschiedenen Konzentrationen beurteilt. Die Nachmodifikation mit organischen Gruppen wurde mittels Infrarotspektroskopie, Zetapotential und Dot-Blot-Analyse untersucht. Die Zytokompatibilität von Eu^{3+}, Tb^{3+} und Gd^{3+} dotierten Partikeln wurden unter Verwendung eines LDH-Assays bewertet. Die Lebensfähigkeit von Zellen mit und ohne NPs nach Bestrahlung mit 150 keV Photonen wurde mittels MTS-Assay und PI-Färbung beurteilt.

Die Ergebnisse zeigen, dass unterschiedliche Synthesewege, einschließlich der mikrowellenunterstützten Synthese, der Präzipitations- und Sol-Gel-Chemie, die Herstellung von Hafniumdioxidpartikeln mit unterschiedlichen physikochemischen Eigenschaften ermöglichen. Darüber hinaus veranschaulichen die Ergebnisse, wie die Lumineszenz- und Röntgenverstärkungseigenschaften durch Dotierung der Hafnia-Matrix verändert werden können und dass die chemische Oberflächenmodifikation eine weitere Anpassung der Zyto- und Hämokompatibilität ermöglicht. Schließlich werden auch vielversprechende radiosensibilisierenden Effekte von Hafnia in einem 2D-Zellkulturmodell gezeigt. Die Wirksamkeit von REE-dotierten Hafnia-Nanopartikeln sollte un wird in verschiedenen in vitro- und in vivo-Modellen, einschließlich Röntgen und Protontherapie, in zukünftigen Studien weiter untersucht werden.

Abstract

Cancer therapy remains a major global issue. While treatment modalities such as surgical resection, chemotherapy, radiotherapy, and thermal ablation have increased patient survival, resistance acquired in the course of the therapy eventually weaken the overall therapeutic success. In order to maximize treatment efficacy and minimize side effects, target cell selectivity is key. The therapy should be delivered exclusively to the tumor cells with minimal effects on healthy tissue. Various approaches have been developed to limit the radiation resistance while simultaneously enhancing the efficacy and safety of radiotherapy.

Nanoparticles (NPs) hold promise as imaging probes and radiosensitizers in order to increase specificity. However, despite much excitement in the scientific community, translation of nanoparticle-based concepts has suffered from significant translational gaps, particularly in the field of biomedicine [23]. Among the nanomedicine-based products which have successfully been commercialized, the majority are based on liposomes. Other marketed nanomedicines include polymeric nanostructures and iron oxide nanoparticles [16, 30, 44].

Among the plethora of nanomaterials with feasible properties, hafnium dioxide has recently attracted attention due to the high dielectric constant ($\epsilon = 25$), high melting point (2758 °C), high atomic number (Z = 72), high density (9.7 g cm^{-3}), high index of refraction, transparency to visible light (5.3–5.9 eV band gap), and chemical inertness. A HfO$_2$ nanoparticle based formulation (NBTXR3, Nanobiotix) used as radiosensitizer has recently been submitted for market approval [44]. However, the understanding of the material properties, and especially its potential as a matrix for multimodal theranostic bioimaging combining x-ray imaging and radiosenzitation with lanthanide doped luminescence and MRI imaging, is vastly limited.

This master thesis is directed towards this gap and investigates the material properties and the potential of hafnia-based nanoparticles for biomedical applications. Undoped and lanthanide doped HfO_2 NPs were synthesized by different methods and subsequently functionalized with PVP, APTES and folic acid. Particle size, shape and morphology was determined by electron microscopy. Composition and crystallinity was measured by x-ray diffraction. Photoluminescent intensities and lifetimes were assessed for Eu^{3+} and Tb^{3+} doped NPs at two different concentrations. Post-modification with organic moieties were investigated using infrared spectroscopy, zeta potential and dot blot analysis. Cytocompatibility of Eu^{3+}, Tb^{3+} and Gd^{3+} doped particles were assessed using LDH assay. Viability of cells with and without NPs after irradiation with 150 keV was assessed using MTS assay and PI-staining.

Results reveal that different synthesis routes, including microwave-assisted synthesis, precipitation and sol-gel chemistry allow preparation of hafnium dioxide particles with distinct physicochemical properties. Furthermore, they illustrate how luminescence and X-ray enhancement properties can be altered by doping of the hafnia matrix, and that chemical surface modification allows further tailoring of the cyto- and hemocompatibility. Finally, positive radiosensibilization effects of hafnia are shown in a 2D cell culture model which make it promising to further investigate the efficacy of REE-doped hafnia nanoparticles in different in vitro and in vivo settings, including X-ray and Protontherapy in future studies.

Contents

Introduction

Different nanoparticle systems have been approved by regulatory agencies and are used in the clinic to either treat or diagnose disease [4]. Their applications are manifold and include iron-replacement therapy, drug delivery, imaging agents and many more. The diagnosis and therapy of a disease, such as cancer, would be much faster, more precise and efficient if different imaging and/or therapeutic agents could be gathered in a single object for multimodal applications [28]. In this regard, new theranostic modalities, i.e. the combination of therapeutic and diagnostic applications, lead the way to optimized and personalized imaging guided therapy [28].

In this masterthesis the potential of hafnia-based nanoparticles (NPs) for multimodal biomedical applications will be explored. Several authors have found different properties of HfO_2 based NPs which show promise for theranostic applications and which are schematically shown in figure 1.1. Particularly the doping of hafnia with rare-earth elements is of interest since the inherent multimodal properties of hafnia can even be further extended. Rare-earth element doped hafnia nanoparticles have prospective applications in X-ray imaging and luminescence imaging but can also act as potent X-ray sensitizers, or active agents in photodynamic therapy. As an example, hafnia NPs can be used as X-ray CT agent as they outperform iodine, a commonly used contrast agent, and perform comparably to gold NPs [45]. Due to a high atomic number it has radiosensitization potential, which was translated

into a product by Nanobiotix (NBTXR3). Lanthanide doped hafnia nanocrystals were found to be photoluminescent making it potentially useful for bioimaging applications and radioluminescent [27] which could be useful in photodynamic therapy (PDT) of deep lying lesions after adaption of the NP's surface. Additionally, doping of the hafnia matrix with magnetic resonance imaging (MRI) active ions, such as Gd^{3+} may render hafnia useful for combined CT and MRI imaging. A challenge still to overcome in generating the next generation of multimodal theranostic nanomedical probes is the effective tumor targeting. At the moment effective particle delivery to tumors is considered to be less than 1% (median) [50].
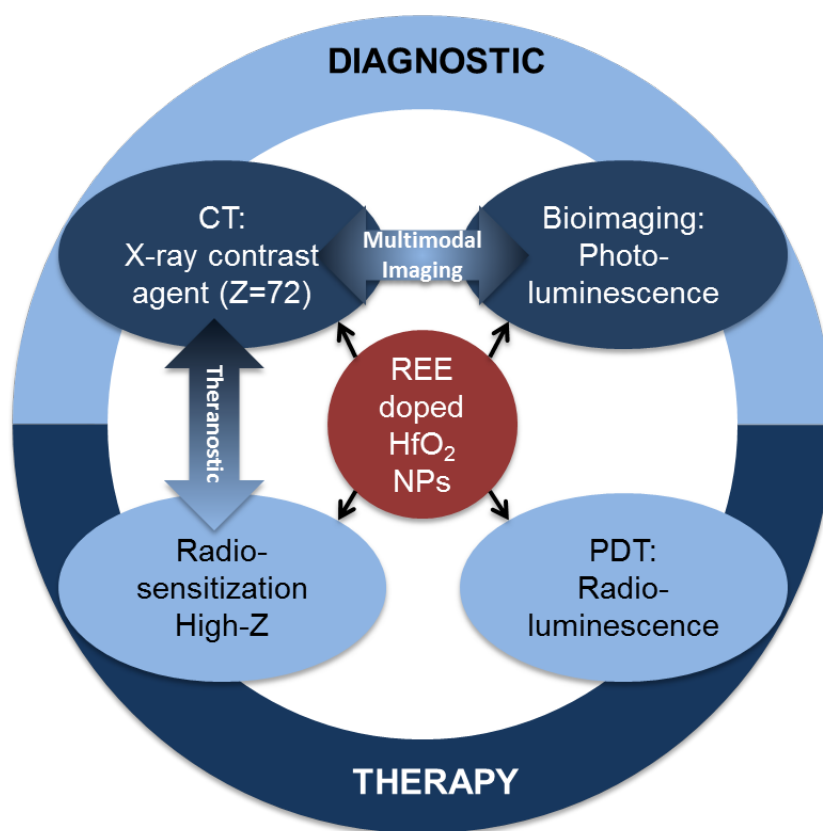

Figure 1.1: Schematic illustration of possible biomedical applications of inorganic rare earth element (REE) doped HfO_2 Nanoparticles (NPs) covering the range of bio- and radiological imaging to cancer therapy.

CHAPTER 2

State of the art

2.1 Hafnium dioxide crystal structure and nanoparticle synthesis

The chemical element hafnium (Hf) belongs to the transition metals and has an atomic number of Z=72. Being tetravalent, together with two oxygen molecules it can form hafnium dioxide. Hafnia (HfO_2) exists in three polymorphs. The stable configuration at ambient pressure and temperature is the monoclinic form, followed by a tetragonal and cubic structure at increasing temperature. The two structures relevant to this work are shown in figure 2.1 together with the crystal parameters. With a Hf^{4+}-atomic radius of 0.78 Å, HfO_2 resembles its twin oxide, zirconia (ZrO_2), in many physical and chemical properties. Its high bulk modulus, band gap, melting point, and chemical stability, as well as the high neutron absorption cross section make hafnia technologically very interesting, for example as gate dielectric replacement of SiO_2 [56]. Due to a higher isoelectric point it is also favourable in biosensor gate dielectrics [13].

The use of HfO_2 in biological systems is underlined by its chemical inertness and the absence of substantial adverse reaction in biological systems like body fluids and tissues [21]. To produce HfO_2 nanoparticles (NPs) several methods have been investigated in the last few years resulting in different shaped and sized NPs. For

3

Phase	No	Site notation	Atom	Multiplicity	Site symmetry	x	y	z	Occupancy	Cell parameters			Cell volume
cubic	1	Hf	Hf	4	m-3m	0	0	0	1	a = 0.51165 nm	b = 0.51165 nm	c = 0.51165 nm	0.1339 nm^3
	2	O	O	8	-43m	1/4	1/4	1/4	1	α = 90 °	β = 90 °	γ = 90 °	
monoclinic	1	Hf	Hf	4	1	0.2764	0.0402	0.2074	1	a = 0.51187 nm	b = 0.51693 nm	c = 0.5297 nm	0.13836 nm^3
	2	O1	O	4	1	0.0709	0.3319	0.3438	1	α = 90 °	β = 99.18 °	γ = 90 °	
	3	O2	O	4	1	0.5536	0.2554	0.0204	1				

Figure 2.1: Overview of structure properties of cubic and monoclinic HfO$_2$ polymorphs. Blue and red dots depict Hf- and O-atoms, respectively; from [52].

example the authors of [36] and [21] have used a precipitation method to produce 6-9 and 20 nm sized monoclinic NPs with band gap values of 4.9 - 6.1 eV. [15], [45] and [37] have used aqueous sol-gel methods yielding monoclinic and cubic NPs with tunable sizes in the range of 4 to 46 nm. Non-aqueous sol-gel methods were used by [27] and [38] resulting in monoclinic and cubic small NPs, with average sizes of 3.1 and 2.6 nm, respectively. Other methods used were hydrothermal and microwave assisted solvothermal routes yielding 12nm [31] and 7 nm sized NPs [14].

2.2 Multimodallity and -functionality concepts for inorganic nanoparticles

2.2.1 Lanthanide luminescence

Lanthanides are rare earth elements (REEs) and comprise 15 elements of the periodic table with atomic numbers from 57 (lanthanum) to 71 (lutetium). They
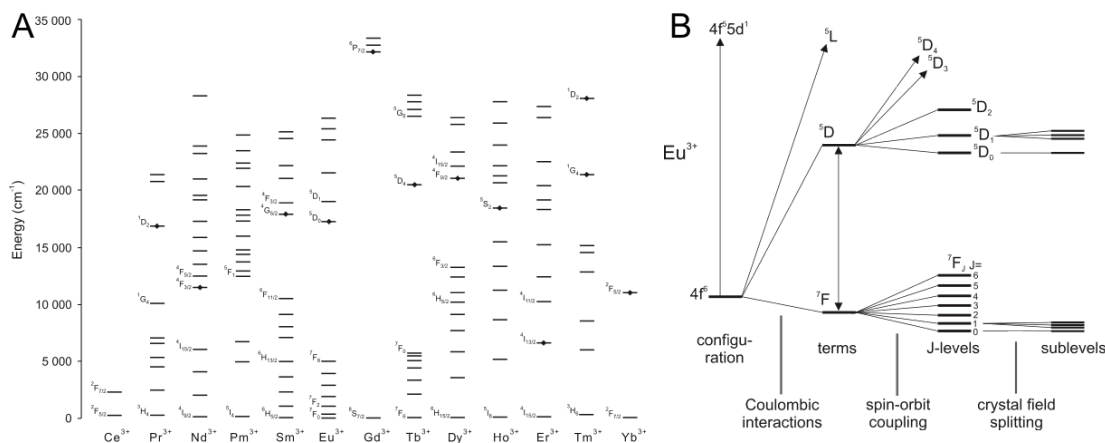
Figure 2.2: A: approximate energy levels for aqueous lanthanide ions. Emittive levels commonly observed are marked with closed tilted squares. B: Representation of Eu^{3+} ion specific electronic energy level splitting due to physical interactions. The electron depopulation of the ^5D level leads to Eu-characteristic photon emission; from [47].

all have valence electrons in the 4f orbitals, apart from lanthanum, which give rise to exceptional photoluminescent properties and by this lanthanides have various applications in bioanalytics and medical diagnostics and imaging. Amongst them, Eu^{3+}, Tb^{3+} and Gd^{3+} ions have the strongest luminescence judged by the energy gap criterion depicted in figure 2.2 (A). Eu and Tb emissions are found in the visible region, while Gd has its emission in the UV region due to a higher band gap. Compared to organic fluorophores, lanthanide based fluorescent reporters have various advantages including (multiple) narrow emission bands arising from split energy levels (see figure 2.2, B), long excited state lifetimes (approximately six orders of magnitude higher) allowing time-resolved detection in bioassays and luminescence microscopy and substantially reduced photobleaching [47].

Luminescence, however, can be used not only for imaging purposes but also for therapy, such as photo-dynamic therapy (PDT). Covering the surface of (nano)particles with photo-sensitizers and using luminescence to activate them creates active molecular species (like free radicals and singlet oxygen) that are toxic to tumors [39]. Rare earth oxides have been shown to be useful for PDT concepts when using X-rays to treat even deep lying lesions [39]. Since REE-doped HfO_2 has been

shown to be photo- and radioluminescent [27], hafnia as a host has potential for multifunctional purposes combining imaging and therapy.

2.2.2   Radiosensitization effect

High-Z materials compared to low-Z, organic materials have a much higher mass energy absorption coefficient [12]. This can not only be advantageous for radioimaging purposes, but also for local dose enhancement. The basic rationale in using inorganic NPs (e.g. gold) as radiosensitizer is for instance explained in [12]. X-ray photons hitting soft tissue loose their energy predominantly by the Compton scattering process, because the probability of the photoeffect is comparably small. The majority of their energy will be retained after collisions and they tend to slow gradually leading to a very sparse distribution of ionizing events. For high-Z NPs, the photoeffect has much more importance (probability $\sim Z^4$), and causes a photon to be absorbed totally to liberate an electron (secondary electron) from the inner shell of an atom. In comparison to soft tissue where binding energies are in the range of 1 keV, inner-shell electrons in for instance gold are bound by 79, 13 and 3 keV depending on the shell. All in all inorganic high-Z NPs absorb substantially more energy per unit mass than soft tissue (compared to gold between 10 and 150 times more for kV photons) which translates to a significant increase in local dose. The secondary electron creation due to increased Compton or photoelectric effect, induces the generation of reactive oxygen species (ROS) by their interaction with surrounding water [34], which also plays a potential role in radiosensitization. Other mechanisms like X-ray triggered drug release and PDT are also considered as radiosensitization effects [39]. The total goal of using NPs in tumor therapy is to increase the differential damage effect between healthy and tumor tissue [39]. Figure 2.3 summarizes the mechanisms and effects of radiosensitization using NPs.

2.2.3   Theranostics

The combination of therapeutic and diagnostic applications is comprised in the word theranostic. It is a rapidly growing field with particular interest focusing on magnetic nanoparticles, such as iron and gadolinium based NPs, especially due to their applicability as MRI contrast agent [2, 19, 28, 32]. MRI, being the principal
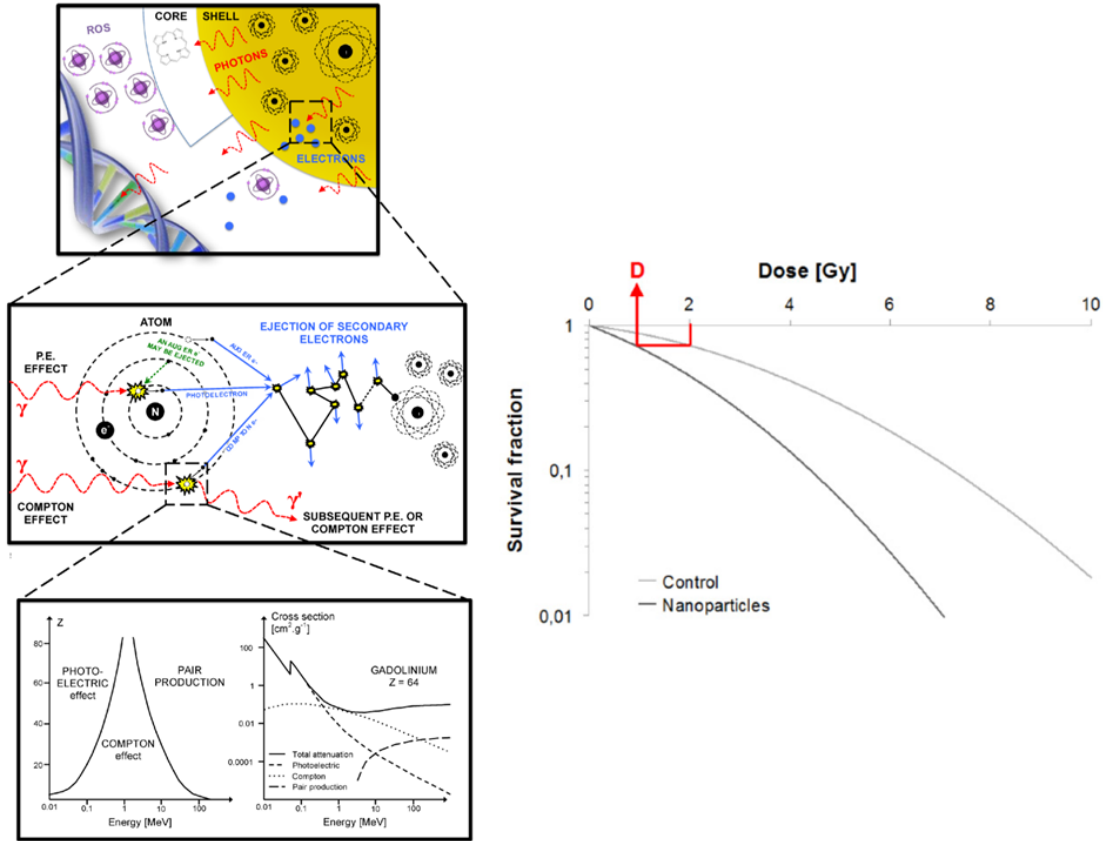
Figure 2.3: Left: direct or indirect production of secondary species (photons, electrons and later ROS) due to interaction of x-rays with NPs lead to increased damage at the site of the tumor. Photoelectric or Compton effect play the major role in secondary photon or electron creation. Right: Illustration of the Dose enhancement due to available NPs. When NPs are present, less dose D is needed for similar survival fractions than without NPs, resulting in a reduced dose in surrounding, healthy tissue; adapted from [39]

oncological imaging modality can be coupled with computed tomography (CT), fluorescence imaging, positron emission tomography (PET) or single photon emission computed tomography (SPECT) for multimodal imaging [28]. Nanoparticulate formulations as contrast agent in comparison with molecular agents benefit from a greater number density at same atomic concentrations, reducing injection dose and potential side effects. This and a higher X-ray attenuation coefficient would make for instance Gd_2O_3 NPs favourable than commonly used iodine contrast agents in CT imaging [2]. However, there are concerns related to Gd^{3+} ion leaching and toxicity. HfO_2 seems to be a promising X-ray contrast agent, too. [45] have shown that hafnia NPs outperform iodine and perform comparably to gold NPs, providing a lower cost alternative to Au NPs. Furthermore, they can be doped with REEs in order to be used in other imaging modalities as well. The therapeutic part can consist of drug delivery, phototherapy, photodynamic therapy (PDT) or different types of irradiation therapies, like neutron therapy, hadron therapy and radiotherapy [28]. The latter would benefit greatly from a contribution of imaging [28] underlining the use of multifunctional NPs in theranostics. A prerequisite for NP applications in diagnostics and therapy is surface modification by biocompatible coatings and functionalization with suitable ligands for targeting cells [19], which is more easily achievable for NPs, than for small molecules [2]. Still, the very low efficiency of nanoparticle delivery to the tumor, which was estimated to be at 0.7% (median) for an administered dose after reviewing the literature from 2006 till 2016 [50], remains a great challenge in translating nanomedicines into clinic.

2.2.4   Hafnium cytocompatibility and clinical use

There are few studies concerning the cytotoxicity of HfO_2 NPs. An early study in 2011 found moderate toxicity to human cell lines as a result of contamination and referred to hafnia by itself as being relatively non-toxic [17]. In 2014 the authors of [21] for the first time performed cytotoxicity study with mouse 3T3 fibroblast cell lines and found no cell damage even at high concentrations of 2.5 mg/mL. Despite the lack of published in vitro cytocompatibility studies, Nanobiotix, developed a novel hafnia based radio enhancer (NBTXR3) for injection into a tumor site designed to undergo cell uptake. With this they have entered phase I clinical trials

in 2011 and have since reached phase II/III for treatment of soft tissue sarcoma. Phase I trials have also begun for different indications and have been completed for rectal cancer in conjunction with PharmaEngine [10].

The approval process for nanomedicines in humans involves several safety assessment phases and is regulated by the Food and Drug Administration (FDA) in the USA, the European Medicines Agency (EMA) in Europe and similar regulatory authorities in other regions. Only a few inorganic NPs have been approved by the FDA. Till 2016, neglecting particles for deficiency (e.g. iron deficiency) indications, only two inorganic NPs, all based on iron oxide, have obtained FDA approval but have already been withdrawn from the market [10]. The Nanotherm product from MagForce, superparamagnetic iron NPs for the local heat treatment of cancer such as glioblastoma, has EU-wide approval since 2010. Others, including gold, iron oxide or C-dots next to NBTXR3 particles, are still in the trial pipeline [10].

Materials and methods
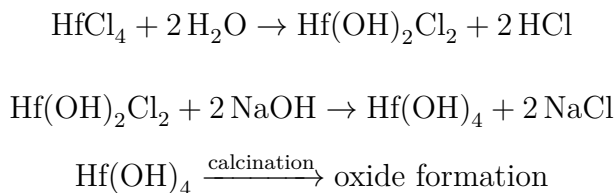
3.1 Nanoparticle synthesis and functionalization

3.1.1 Materials

Hafnium(IV) chloride (99.9% trace metal basis), Terbium(III) nitrate hexahydrate (99.999% trace metals basis), Europium(III) chloride hexahydrate (99.99% trace metals basis) and Gadolinium nitrate hexahydrate (99.99% trace metals basis) were purchased from Sigma Aldrich. (3-Aminopropyl)triethoxysilane (APTES, 99%, 440140) and Polyvinylpyrrolidone (PVP360) for surface functionalization were also purchased from Sigma Aldrich.

3.1.2 Precipitation method

For the synthesis of HfO_2 NPs via a precipitation route the method of [21] and [36] was used. In principal an aqueous solution of 0.4M NaOH was added drop wise to the same volumetric amount of 0.1M $HfCl_4$ and the solution was stirred magnetically with a Teflon coated bar over night. Afterwards, the solution was centrifuged ($>$ 4000rpm) and washed three times with Milli-Q water to get rid of any trace impurities. The resulting white colored gel, after discarding the supernatant, was

dried in an oven for three hours in air before it was calcined for 2 hours at 500°C. Following the cool down, the sample was mortared with an Achat mortar and pestle to yield a white powder. For doped samples the appropriate molar amount of Terbium(III) nitrate hexahydrate or Europium(III) chloride hexahydrate was dissolved in the aqueous $HfCl_4$ solution before adding the aqueous NaOH solution. The basic reaction can be written as:

$$HfCl_4 + 2\,H_2O \rightarrow Hf(OH)_2Cl_2 + 2\,HCl$$

$$Hf(OH)_2Cl_2 + 2\,NaOH \rightarrow Hf(OH)_4 + 2\,NaCl$$

$$Hf(OH)_4 \xrightarrow{\text{calcination}} \text{oxide formation}$$

3.1.3   Microwave-assisted precipitation method

For the microwave-assisted synthesis of HfO_2 NPs, the same procedure was used as for the precipitation route. However, after mixing and stirring of the precursors, the Hafnium-hydroxide solution was put into a glass microwave tube and was microwaved for three hours at 120°C with a maximum power of 1200 W. After cooling down to room temperature, the precipitate was washed and centrifuged at 8000 rpm for 20 min 3 times, to get rid of impurities. Then the precipitate was dried at 80°C for 24 hours.

3.1.4   Sol-Gel method

The Sol-Gel method was done according to previous reports [18, 37, 45]. In short, 0.05 mol of citric acid was added to 24 mL pure Water to yield roughly 31 mL of 2 M aqueous citric acid solution. To this, 2 g (0.00625 mol) of $HfCl_4$ (or $Gd(NO_3)_3 \cdot 6H_2O$ for Gadolinium Oxide) was added and magnetically stirred over night. On the next day, 0.2 mol of ethylene glycol (1:4 ratio of citric acid:ethylene glycol) was added to the polymer metal precursor while stirring in an oil bath at 90°C. The high temperature was used to support polyestherification and was kept for three hours. To get rid of all water, the final more viscous but transparent solution was dried at 130°C over night. After the drying step, the resulting dried gel was calcinated in a preheated oven at 600°C for 2 hours to burn off all organic elements

and yield a white powder (yellow in terms of terbium doping). For doped samples the appropriate molar amount of doping precursor was added to the citric acid solution.

3.1.5 Surface functionalization

PVP surface functionalization was done by adding 1 wt% PVP to a Milli-Q solution containing roughly 60-80 mM as synthesized HfO_2 powder and stirring over night, using a teflon coated magnetic bar.

APTES surface functionalization was done by adding 4 mL ammonia hydration to 0.5 g of Hafnia nanoparticles suspended and sonicated in 16 mL Milli-Q water. Ethanol was added until the total volume was 150 mL. The mixture was stabilized with an oil bath at 30°C. Then 25 µL of APTES was added under stirring and the mixture was allowed to react overnight. Thereafter, unreacted APTES was removed by washing with ethanol or milli-Q water and centrifuging at 7000 rpm for 30 min for at least 3 times, before it was suspended in ethanol or water.

3.2 Nanoparticle characterization

3.2.1 X-Ray powder diffraction (XRD)

The analysis of the crystal structure was performed using a Stoe Mark II-Imaging Plate Diffractometer System (STOE & Cie GmbH, Darmstadt, Germany, 2015) equipped with a graphite-monochromator at the Center for X-ray Analytics Empa Dübendorf, Switzerland. Diffraction patterns are collected using $Mo-K\alpha$ radiation ($\lambda = 0.71073$ Å, beam diameter 0.5 mm). Two-dimensional diffraction images (10 min exposure time) were obtained at an image plate distance of 200 mm with a continued sample rotation and Intensity integration over the entire image (360°). The resolution was $D_{min} = 24.00$ Å - $D_{max} = 1.04$ Å. Crystallite sizes were estimated by applying the Scherrer equation to the (-1-11) peak at $2\theta = 12.9°$ for monoclinic and to the (111) peak at $2\theta = 13.8°$ for cubic phases.

13

3.2.2 Transmission electron microscopy (TEM)

Nanoparticle morphology was assessed using a JEOL 2200FS TEM operated at 200 kV for diffraction contrast imaging and selected area electron diffraction (SAED).

3.2.3 Dynamic light scattering (DLS) and zeta potential

Measurements to assess hydrodynamic size and surface charge have been done using a Zetasizer Nano ZS90 (Malvern Instruments Ltd., Worcestershire, United Kingdom) with a 90°scattering angle. The colloid concentration (particles in Milli-Q water) for size measurements used was 1 mg/mL so that the attenuator was around 8 and the derived count rate was between 4000 and 5000 kcps. The refractive index for Hafnium dioxide n = 2.1 was collected from the database [33]. The viscosity of water was used for the colloid. The particles were sonicated using a Branson Digital Sonifier Type 450 (Branson Ultrasonics, Danbury, USA) with a 3/4" High Gain Horn for 10 min, using 70% amplitude and a duty cycle of 3:1. The colloid was cooled in an ice bath and DLS was measured within 10-20 min using 3 replicate measurements. Only one sample (pure HfO_2) was sonicated longer, as it was not stable enough after the first sonication cycle. Functionalized particles, in order to not destroy the surface with the high power tip sonicator, were put in a sonication bath up to 60 min prior to DLS measurements.

For zeta potential the particle concentration was adjusted to 1 mM and PBS was added, such that the total volume contained 10% PBS. The Attenuator was found to be 6 (7 in only one sample: HfO_2:10%Eu). The conductivity was in all cases around 2 mS/cm, except for the PVP functionalized sample, where it was around 1 mS/cm. Additional to the Dynamic Light Scattering technique, Nanoparticle Tracking Analysis was used to assess particle sizes (NanoSight NS500, Malvern Instruments Ltd., Worcestershire, United Kingdom).

3.2.4 Attenuated Total Reflectance (ATR)

ATR was measured using a Varian 640-IR Spectrometer to assess vibrational surface states. The samples were mortared with a Achat prestle and mortar prior to measuring.

3.2.5 Photoluminescence

Photoluminescence spectra were measured at room temperature using a Varian Cary Eclipse Fluorescence Spectrophotometer. The excitation light source was a xenon lamp with build in monochromator grating. Steady state emission and excitation spectra were taken under phosphorescence mode, with a delay time of 0.1 ms, a gate time of 5 ms and a total decay time of 10 ms. For time resolved photoluminescence the decay signal of 544 nm under 267 nm excitation for Terbium doped samples, and the 612 nm emission under 230 nm excitation for Europium doped samples were studied. The concentration of the measured sample colloid was 1.1 mg/mL. The sample powder was dispersed in Milli-Q water, sonicated with a micro-tip sonicator for 4 min at 30% amplitude and 40% duty cycle, and dipped into a sonication bath prior to measuring.

3.2.6 Dot plot

Dot-Blot Immunoassay was performed at room temperature like in [3]. FA-functionalized and APTES-functionalized (without FA) NPs were deposited at the same concentration (1mg/mL) on an absorbent filter paper (Bio Dot SF Filter Paper, Bio Rad), which was cut in round circles fitting in a 48 well plate. 5 µL drops were added slowly. Subsequent increases in NP amount were performed by adding another 5 µL until 3 different amounts of NPs were available with minimum 5 and maximum 15 µL NP suspension. After drying, nonspecific sites in the membranes were blocked by soaking in0.6 mL 5% (w/v) BSA (bovine serum albumin) in TBST (20mM Tris-HCL, 150mM NaCL, 0.05% (v/v) Tween20, pH 7.6).for 1 h on a shaker. After discarding the blocking solution 0.12 mL of monoclonal antifolic acid primary antibody () diluted 1:500 in 5% BSA in TBST was added to the membranes for 1 h. The membranes were washed 3 times for 5 min in TBST. Then goat anti-mouse IgG secondary antibody (Alexa Fluor 488 or 633) diluted 1:200 in TBST was added to the membrane for 1 h in the dark. Afterwards, the membrane was washed again with TBST 3 times. The well plate with the membranes was protected from light until fluorescence was measured using a microplate reader or it was imaged using a TECAN LS Reloaded microarray reader.

3.2.7   Elemental analysis

Elemental analysis by inductively coupled plasma atomic emission spectroscopy (ICP-OES) was conducted at EMPA, St. Gallen. Total digestion of Hafnia NPs was done at 180 °C and by using 1 ml HF, 1ml HNO_3 and 1 ml H_2O.

3.2.8   Ion leaching

1 mg/mL of particles (HfO_2; HfO_2:10%Tb or HfO_2:10%Gd) were dispersed in K-citrate buffer and prepared by sonication (2 min; 70% amplitude; 3:1 duty cycle; micro tip). The 100mM K-citrate buffer was prepared using citric acid and potassium citrate such that the pH was 4.5 (lysosomal pH). The NP-suspension was aliquoted into volumes of 1.5 mL and analyzed or put on a shaker in a 37°C room for 1 day. 3 aliquots of each condition were used for elemental analysis. The analysis samples were centrifuged at 20000 g for 20 min. 0.8 mL of supernatant was collected and stored in a freezer at -20°C. On measuring day, supernatants were thawed and diluted 10 times in HNO_3. Standards (suspension liquid diluted in HNO_3), as well as positive controls (Tb, Gd, Hf ions in suspension liquid at two concentrations) were prepared for calibration and measured.

3.3   Cell handling and in vitro experiments

3.3.1   Cell lines and culture conditions

The Caco-2 cell line (ACC169) was acquired from 'Leibniz Institute DSMZ-German Collection of Microorganisms and Cell Cultures' (Braunschweig, Germany). Undifferentiated cells were grown in Minimum Essential Medium Eagle (MEM, Sigma-Aldrich, M2279) with 10% Fetal Calve Serum (FCS, Sigma-Aldrich, F9665), 1% L-Glutamine (Sigma-Aldrich, G7513), 1% Penicillin-Streptomycin-Neomycin (PSN, Sigma-Aldrich, P4083) and 1% Non-Essential Amino Acids (Sigma-Aldrich, M7145) in addition. They were maintained in an incubator at 37 °C under 5% CO_2 humidified atmosphere. Routinely sub-culturing was done twice a week at 70-80% confluence by treatment with 0.5% Trypsin-EDTA (Sigma-Aldrich, T3924). The THP-1 cell line (TIB-202) was acquired from American Type Culture Col-

lection. THP-1 cells were grown in suspension and routinely subcultured once a week in RPMI-1640 culture medium (Sigma-Aldrich, RO883) with 10% FCS, 1% L-Glutamine and 1% PSN in addition.

3.3.2 TEM sample preparation and imaging

For imaging particles in cells with electron microscopy, 0.5 Mio Caco-2 cells were seeded in a 6 well plate and 0.1 mg/mL particles were added on the next day. After washing with prewarmed PBS and trypsinizing, cells were incubated for 2.5 h at room temperature in 4% methanol-free paraformaldehyde (PFA). The cell pellets were washed 3 times with ddH$_2$O, twice with cacodylate buffer (0.1 M) and then stained with 2% osmium tetroxide and 1.5% potassium ferricyanide for 1 h. Afterwards, they were gradually dehydrated using an ethanol gradient (50%, 60%, 70%, 80%, 90%, 100%, 100%, 1000%) and embedded in epoxy resin (EPON 812), first together with ethanol (50%) for 10 h and then pure for 3 days in the fridge. Resin blocks were then cured in the oven, trimmed with a razor blade, sectioned in 100-nm slices using an ultramicrotome and imaged in a JEOL 100 Plus TEM at 80 keV.

3.3.3 Cytotoxicity assay

LDH assays were performed based on protocols from the manufacturer for the CytoTox 96®Non-Radioactive Cytotoxicity Assay (Promega Corporation, USA). In short, 5000 cells were seeded into the wells of a 96 well plate with 225 µL supplemented culture medium and incubated for 24 hours at standard culture conditions. To measure the cytotoxicity of particles, 25 µL of according aqueous particle concentrations (1, 2.5, 5, 10 mg/mL) were added to each well after 2 min tip sonication, so that the maximum amount of H$_2$0 was 10%. Cells were then incubated for 24 hours. Thereafter, 50 µL of the supernatants were transferred into a new 96 well plate. 50 µL CytoTox 96®Reagent was added and the plate was incubated at room temperature in the dark for 30 min. 50 mL stop-solution (Promega, G183A) was added and the absorbance was measured at 490 nm with a microplate reader. The data was analyzed by subtracting the background, i.e. the average of 3 wells filled with 100 µL Medium and LDH reagent, from all absorbance values and divide

this by the positive control with maximum LDH-release, which was the average of three wells with cells treated with 25 µL of 1% Triton X-100 (Sigma-Aldrich, X-100) in Dulbecco's Phosphate Buffered Saline (DPBS; Sigma-Aldrich, D8537) and 225µL supplemented MEM.

3.3.4   Hemocompatibility

Hemolysis and **coagulation** assessment was done like in [29]. Whole blood drawn from healthy volunteers using 0.109 mol/L citrate as an anti-coagulant. The blood was centrifuged at 2000g. The plasma was removed and used for the coagulation assay. Red blood cells were resuspended in PBS, washed three times and the hemoglobin concentration was adjusted to 30 mg/mL. For the measurement 180 µL red blood cells and 20 µL of nanoparticle suspension (undoped, doped and functionalized NPs) were added to Eppendorf tubes yielding a final NP concentration of 0.1mg/mL and incubated for 3 h at 37 °C. Positive and negative control used 1% Triton X solution and PBS, respectively. After centrifugation at 6000g for 5 min 100 µL of supernatants were transferred to a 96-well plate and absorption at 570 nm (hemoglobin) was measured with a Mithras^2 LB 943 multimode microplate reader.

For **coagulation** experiments 20 µL of the same nanoparticle suspensions were added to tubes containing 180 µL blood plasma, incubated at 37 °C for 30 min and centrifuged at 6000g for 5 min. Supernatants (100 µL) were transferred to 96-well plate, recalcified with 65 µL of 50 mM $CaCl_2$ solution and absorbance was measured at 405 nm in 50 s intervals during 1 h with a plate reader (Mithras^2 LB 943) to assess fibrin polymerization. Fumed silica (A200) was used as reference for fast blood clotting time reaching early clotting saturation.

3.3.5   Cell irradiation conditions and analysis

For cell irradiation experiments, 200000 Caco-2 cells were seeded in 12 well plates (only a square with 3×3 wells was used) in 0.9 mL supplemented MEM 48 h prior to the irradiation. After 24 h incubation at usual conditions 0.1 mL of 5 mg/mL particle suspension (HfO_2 and HfO_2:10%Tb) in milli-Q water was added, so that

the final NP concentration was 0.5 mg/mL/(4 cm^2 growth area). For cells without NPs, 0.1 mL of milli-Q H$_2$O was added. At irradiation day, cells were transported in the car to EMPA, Dübendorf, where cells were irradiated with 150 keV photons (source) reaching 1 Gy/min. An aluminium foil (1.2 cm thickness) was placed above the cell well plate, to filter out low energy photons and a dosimeter was placed next to the plate. For each condition 3 replicates were done. Positive controls were cells with 0.1% Triton X or 100 µM CdSO$_4$. Negative controls were cells without NPs seeing no radiation. After irradiation with different doses, cells were put on ice and transported back to EMPA, St. Gallen.

For **flow cytometric analysis (FACS)** the supernatant of the cells was discarded after centrifugation at 200g for 10 min and 400 µL Facs buffer and 5 µL Propidiumiodid (PI) was add and measured immediately with a Beckmann & Coulter Gallios TM Flow Cytometer. Fluorescence was measured at channel 4 (FL4) and analysis was done with Kaluza Analysis software.

For **MTS measurements**, the same amounts of cells in media corresponding to 5000 cells of healthy control were reseeded into a 96 well plate and after 5 days MTS evaluation was done. For this the old medium was replaced with 120 µL of MTS working solution, consisting of 20 mL phenolred free MEM and 4 mL MTS (CellTiter 96® AQ$_{ueous}$ One Solution Cell Proliferation Assay, Promega). Cells were then incubated at standard conditions for 1 h, before measuring the absorbance at 490 nm in a plate reader. For the analysis, the absorbance of the negative control was subtracted from all absorbance values. Then, the values were divided by the average absorbance of the positive control. The nanoparticle-mediated enhancement factor (NER) for one dose was calculated by

$$NER = \frac{\text{viability of irradiated cells with NPs}}{\text{viability of irradiated cells without NPs}}.$$

Results and discussion

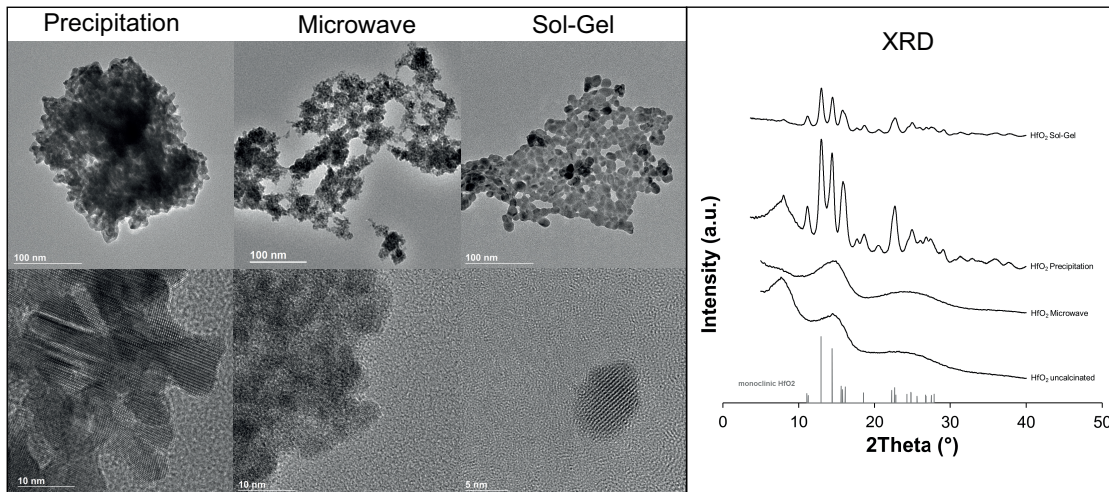## 4.1 Synthesis and characterization of hafnium dioxide nanoparticles

Figure 4.1: Overview of TEM pictures (left) and XRD spectra (right) for HfO$_2$ Nanoparticles synthesized by different methods. Monoclinic XRD reference spectrum given by [1]

Hafnia (hafnium dioxide) NPs were synthesized by three different methods reported in the literature. Figure 4.1 depicts the TEM images of hafnium dioxide nanopar-

ticles (NPs) synthesized by precipitation, microwave assisted precipitation and sol-gel methods. Each synthesis method was successful and led to the formation of nanoparticles (NPs) with sizes of around 10 nm. The microwaved particles seem to be smaller, but have an amorphous phase. For these particles high resolution TEM pictures show only diffuse structures, making it challenging to identify single particles between agglomerated particles and to extract NP size. This is confirmed by the broad humps in the XRD spectra (shown in the same figure). Precipitated particles seem to have irregular shapes (e.g. elongated, elliptical or spherical). Before calcination, precipitated particles are amorphous as seen in the XRD spectra. It can be concluded, that calcination at 500 °C induces a transformation into a monoclinic crystal phase. The NPs obtained by the sol-gel method are predominantly of ellipsoidal shape. XRD confirms a monoclinic crystal phase after 2 h calcination at 600°C. While all samples show agglomerated NPs, it was possible to find single NP crystals in the sol-gel sample (figure 4.1). The better discriminability, less dense aggregation, good crystallinity and the observation of single NPs make the sol-gel method the preferred route for further modifications and the use in biomedical applications.

4.2 Synthesis and characterization of Tb^{3+} and Eu^{3+} doped photoluminescent hafnium dioxide nanoparticles

To investigate the potential of hafnia as a host matrix for guest ions, HfO_2 NPs were doped with different REEs, including Tb^{3+} and Eu^{3+}. XRD spectra for different synthesized undoped and doped HfO_2 NPs are shown in figure 4.2. Interestingly, after heat treatment at 500 and 600°C crystalline spectra for precipitated and sol-gel samples are observed. However, there are two different phases, monoclinic and cubic, detected. Especially those particles doped with 10% of trivalent atoms (10% Eu or Tb) show a cubic phase regardless of synthesis method, with one exception, which is the precipitated 10% Eu doped HfO_2. In this sample, both phases are observed, which might hint to an unsuccessful incorporation of doping ions. For lower amounts of doping, both phases co-exist. Therefore, it can be

suggested, that doping induces a crystallographic phase change of monoclinic HfO₂, with a stabilized cubic phase at 10% trivalent dopant.

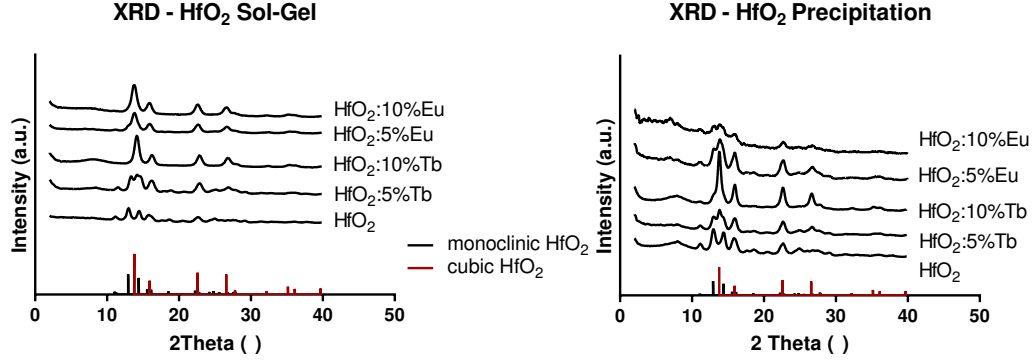Figure 4.2: Overview of XRD patterns for HfO₂ doped and undoped HfO₂ nanoparticles synthesized by different methods; monoclinic reference data from [1]; cubic reference data from [24].
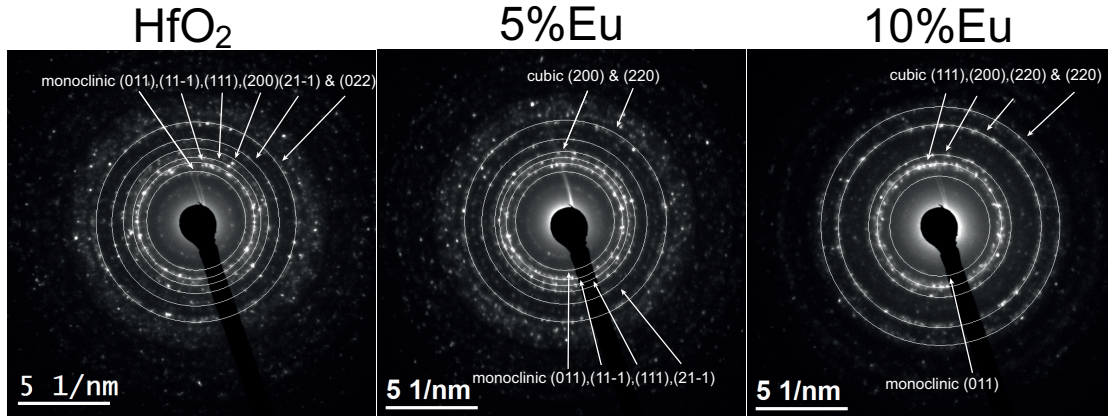

Figure 4.3: Selected SAED patterns for HfO₂ Nanoparticles synthesized by sol-gel method, undoped and doped with 5% and 10% europium. Diffraction rings are indexed using the Database from [52] for monoclinic and cubic HfO₂. The corresponding d-spacings are listed in table 4.1. The planes for doped hafnia NPs (middle and right) are compared to the undoped HfO₂ NPs (left).

The changes in crystal structure have been further investigated by selective area electron diffraction (SAED). Diffraction patterns allow distinction between amor-

phous and crystalline phase. Furthermore, they can make differences in crystal structure visible. For all crystalline phases well defined diffraction spots can be found from which the crystallographic planes can be indexed. Figure 4.3 shows the indexed crystal planes for sol-gel synthesized HfO_2 NPs undoped and doped with 5 and 10% europium. The ring patterns suggest the presence of randomly-oriented nanocrystals. The spottiness of the rings indicate either a small number of these crystals or a large crystal sizes. Measuring the diameter of the diffraction rings gives the spacing of the reflecting planes. Table 4.1 compares the indexed measured d_{hkl} spacings with the database from [52]. It can be seen, that for an increasing amount of trivalent dopant into the fourvalent matrix the diffraction pattern changes. While the HfO_2 NPs are in good agreement with the monoclinic polymorph, the 10% Eu doped NPs compare well to the cubic polymorph. In fact, it seems that the (11-1) and the (111) plane merge into each other. This would be indicative for the higher symmetry, cubic phase, since these planes are diagonal planes from the same {111}-family in a cubic cell. The 5% Eu doped NPs show predominance of the monoclinic phase.

Phase	hkl	d_{hkl} - spacing (nm) of HfO_2			
		Database	0% Eu	5% Eu	10% Eu
Monoclinic mP12	011	0.3676	0.3696	0.3696	0.3656
	11-1	0.3145	0.3148	0.3148	-
	111	0.2826	0.2857	0.2857	-
	200	0.2527	0.2524	-	-
	21-1	0.2201	0.2198	0.2222	-
	022	0.1838	0.1835	-	-
Cubic cF12	111	0.2954	-	-	0.2957
	200	0.2558	-	0.2576	0.2576
	220	0.1809	-	0.1818	0.1802
	311	0.1543	-	-	0.1539

Table 4.1: Interplanar d_{hkl}-spacings of monoclinic and cubic HfO_2 with corresponding miller indices (database values from [52]). All monoclinic and cubic planes indexed in figure 4.3 for HfO_2 NPs are shown.

The above data is an indirect proof, that the incorporation of doping ions was successful, indicated by the phase change. For a direct proof and, moreover, to show the amount of contained doping ions, ICP-OES analysis of dissolved NPs was done. Table 4.2 shows the amount of dopant measured in the NPs using ICP-MS as well as the prevalent crystallographic phase and the crystallite size. With this, the phase

Synthesis method	Sample description	Prevalent crystallographic phases	Crystallite size	molar percentage of dopand theoretical	experimental
	HfO2	monoclinic	8(2)nm	-	-
	HfO2:5%Tb	monocl. and cubic	*	5.1%	1.6%
Precipitation	HfO2:5%Eu	monocl. and cubic	*	5.4%	1.0%
	HfO2:10%Tb	cubic	9(2)nm	10.5%	10.2%
	HfO2:10%Eu	monocl. and cubic	*	10.3%	3.9%
	HfO2	monoclinic	9(2)nm	-	-
	HfO2:5%Tb	monocl. and cubic	*	5.3%	4.0%
Sol-Gel	HfO2:5%Eu	monocl. and cubic	*	7.0%	4.1%
	HfO2:10%Tb	cubic	6(2)nm	11.1%	7.3%
	HfO2:10%Eu	cubic	5(2)nm	12.4%	10.7%

* As peaks of different crystallographic phases are superposing, the Scherrer equation can't be used to estimate the crystallite size.

Table 4.2: Overview of crystallographic phases and sizes. Monoclinic and cubic phases refer to Pearson symbols mP12 and cF12 for HfO$_2$2 materials, respectively. Indicated additionally is the nominal molar percentage of dopant provided by ICP-OES measurements (experimental) and the theoretical one, which is the amount of dopant added during synthesis.

change observed by XRD can be correlated to the dopant amount. It seems that the minimum amount for having a prevalent cubic phase is between 5 and 8 mol%. This is also the reason, that the XRD pattern of the precipitated 10% Eu doped HfO$_2$ shows no stabilized cubic phase. Instead of 10 mol% it contains only 4 mol%. Generally, the deviation of doping amount found experimentally compared to the expected amount is higher for precipitated particles (mean deviation 54%) than for sol-gel particles (mean deviation 28%), highlighting that also for the incorporation of REEs the sol-gel method is the preferred method. The cubic phase stabilization due to trivalent ions was also seen by other authors. [27] have set the threshold above 5 mol%, as they have found a phase change at 6.5 mol% Eu doping for a nominal 8 mol% HfO$_2$ doped sample. [22, 38] state that the phase change due to the trivalent ion incorporation is stabilized by the generation of structural oxygen vacancies for charge compensation. [38] further was able to stabilized the cubic phase even without using dopants but a reductive environment during synthesis. Taking XRD and SAED patterns in figure 4.3 into account, it is obvious that a phase change has happened with doping, but even at 10 mol% the cubic phase hasn't stabilized to 100% and monoclinic phases are present as well to minor extent. Accompanied by the phase change is a decrease in crystallite size from 9 ± 2 nm to 6 ± 2 nm for the sol-gel synthesized samples. The images done by TEM affirm the sizes analyzed by XRD. [15] have also found 9 nm monoclinic crystallites with similar synthesis conditions and the sol-gel method. Changing from a monoclinic to a cubic lattice seems to decrease crystallite size in the hafnium NPs (table

4.2). The size change cannot be explained only by a cell volume decreases of 3 - 4 %, from 0.13836 to 0.1339 nm^3. While it is known, that annealing increases the crystallite size [15, 27] the influence of doping on size is not fully clear. [27] for example have found no size decrease, but a regular size distribution for 3 nm sized NPs, irrespective of the REE doping levels which ranged from 0 to 10 mol%.

The incorporation of europium and terbium ions into the HfO_2 NPs give rise to luminescent properties in the visible region, which have been detected and which are shown in figure 4.4. The emission intensities after excitation with light in the UV-spectrum are related to the dopants and their energy levels. The emission lines at 490, 544, 588 and 622 nm originate from the $^5D_4 \rightarrow^7 F_{6,5,4,3}$ transitions within the the $4f$ electron configuration of terbium (figure 4.4, A). Interesting to note is that with 10% Tb doping the emission, as well as excitation intensities are about a factor of 4 higher than for 5% doping. The maximum excitation intensity for the Tb emission at 544 nm is found at 267.2(2) nm (4.640(4) eV) and 268.7(2) nm (4.614(3) eV) for 10 and 5% Tb doping, respectively (after Gaussian fit within 95 confidence interval). The more energetic but smaller excitation peaks are found at 221.1(8) nm (5.61(2) eV) for 10 % and 229.5(7) nm (5.40(2) eV) for 5% dopant, which is close to the reported band gap value of 5.7 eV for hafnium dioxide [51]. These bands are referred to as conduction bands (CB) of the host lattice. The blueshift in the CB with increased Tb concentration can be attributed to the doping induced decreased size and thus to the quantum confinement effect [11]. The lower energetic peaks are most probably the charge transfer bands (CTB) and are attributed to an $O^{2-} \rightarrow Tb^{3+}$ electron transfer reducing Tb^{3+} formally to Tb^{2+}, similar to the situation found in Europium [9, 11]. Europium emission lines and profiles at 592, 612, 630, 654, 712 and 746 nm (figure 4.4, B) correspond to the $^5D_0 \rightarrow^7 F_{1,2,3,4,5}$ transitions [9]. Differently to Tb doped NPs, here the luminescence intensity is reduced with the higher level of doping. The maximum emission intensity of the $^7F_2$ peak is hypersensitive to its environment and differs slightly for 5% (612 nm) and 10%Eu (609 nm) doped HfO_2 NPs. Also the maximum excitation intensity is shifted due to doping (figure 4.4, C). The higher and lower Eu doped NP crystals and their $^5D_0 \rightarrow^7 F_2$-emission are maximally excited at 240.4(2) nm (5.157(4) eV) and 231.6(3) nm (5.353(7) eV), respectively. These peaks might be referred to as
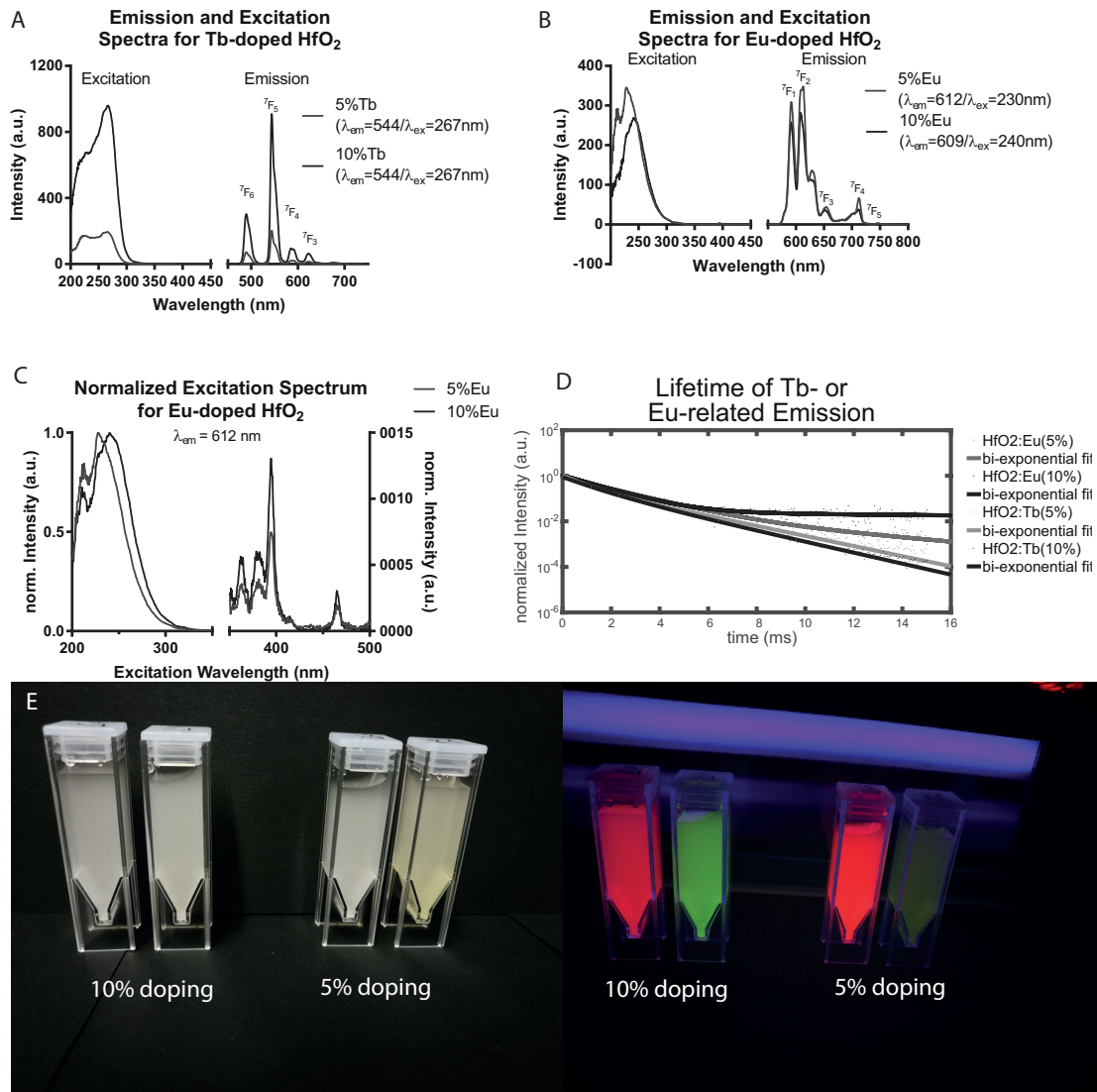
Figure 4.4: Emission and excitation spectra for 5 and 10% terbium (A) and europium (B) doped HfO$_2$ NPs using maximum excitation (λ_{ex}) and emission (λ_{em}) wavelengths. Normalized excitation spectra for Eu doped NPs (C) are normalized towards the excitation maximum using the same emission wavelength of 612 nm. Lifetimes of the 612 nm and 544 nm emission peaks for Eu and Tb doped NPs (D). Photometric picture of the Eu and Tb doped NP colloids in the dark and under UV light exposure (UV lamp Benda NU-8 KL; 2 × 8 Watt; 254 and 366 nm excitation) (E).

charge transfer bands. The higher lying bands at 208.0(2) nm (5.961(6) eV) for 10% and 209.5(3) nm (5.92(1) eV) for 5% Eu doping would then be the CBs. A redshift phenomena of the CTB and a blueshift of the CB was also found by [11] in 1 mol% Eu doped Y_3O_2 for decreased annealing temperatures, which was explained by a decreased crystallite size. [21] have also found a blue shift of the energy gap with decreased size of HfO_2 nanoparticles. However, reported values for the energy band gap range from 5 to 6 eV [7] and, therefore, the here observed excitation bands lie within the band gap energy range for HfO_2. The band arrangement is crucial for luminescent properties as proposed by [48], because it defines which energy process is involved, either phonon assistant energy transfer (CB higher than CTB), resonant energy transfer (CB and CTB levelling), or energy back transfer process (CB lower than CTB). The latter process would lead to quenching and reduced luminescence, as observed here. Due to the smaller crystallite size found by XRD for Eu compared to Tb doped HfO_2 a higher energy gap is expected, proposing that the higher excitation peak at 5.9 eV is coming from the CB. This proposition implies that another quenching effect is responsible for luminescence decrease at higher Eu doping. Concentration quenching is a known effect in rare earth doped semiconductors. When dopant distance is decreased there is an increased probability to reach a path of non-radiative decay and the excitation energy is transferred between many ions in the time necessary for the radiative decay [6]. This effect was not observed in Tb doped HfO_2 NPs.

Much weaker than the CTB in the excitation spectrum in figure 4.4, C, are the europium characteristic excitation lines attributed to the intraconfigurational 4f transitions of the Eu ions [9]. These intensities show an opposite behavior, an increased excitation with increased dopant since more Eu atoms are incorporated into the HfO_2 matrix and available. The low intensities observed suggest a more efficient photoluminescence via photoabsorption of the host lattice and transfer to the dopant ions.

Time-resolved measurements of the most intense Eu and Tb emissions show life times in the range of milliseconds. Figure 4.4, D, shows the bi-exponential curve fits to the time resolved emission data. From these, the mean life times were calculated

using

$$\langle \tau \rangle = \frac{\sum\limits_{i=1}^{2} \alpha_i \tau_i^2}{\sum\limits_{i=1}^{2} \alpha_i \tau_i},$$

where α_i represents the pre-exponential factors and τ_i the individual life times. Uncertainty propagation was calculated using the 95% confidence interval from the exponential fit. For 5% and 10% Eu doped NPs the mean lifetimes are $\langle \tau_{5Eu} \rangle = 0.582(56)ms$ and $\langle \tau_{10Eu} \rangle = 0.725(62)ms$. These are slightly shorter than the 1.2 ms lifetimes observed in Eu doped 200nm thin HfO$_2$ films by [26], but much higher than the 3 ns lifetimes observed in precipitated 12 nm sized Eu doped HfO$_2$ NPs by [46]. For Tb doped NPs the lifetimes are slightly longer, $\langle \tau_{5Tb} \rangle = 1.29(31)ms$ and $\langle \tau_{10Tb} \rangle = 0.947(79)ms$. The relatively long decay time makes Eu and Tb doped HfO$_2$ NPs a good candidate for time-resolved biomedical applications. In this regard the excitation energies must, however, be tailored towards lower energies in order to decrease toxicity from excitation wavelength. A possible mechanism would be the up conversion from infrared light, which could also be useful for photodynamic therapy, and which has been observed for different hosts and combinations of REEs [43, 49, 53–55].

A visualization of the strong photoluminescence of Tb and Eu doped HfO$_2$ NPs was done by exciting a colloid under a UV lamp. A photo was taken and is shown in Figure 4.4, E. Doping concentration effects are coinciding with the results from the spectral analysis. In total, hafnium dioxide has been shown to be a good host for the incorporation of REEs.

4.3 Colloidal sizes of hafnia based nanoparticles

In order to use (Nano)particles in biomedical applications suspension stability and size play a crucial role. Cell uptake, toxicity and NP functionality are influenced also by NP size. TEM images already showed aggregation effects. Dynamic light scattering (DLS) was used to assess the average sizes of NP agglomerations in water. Additionally to the hafnia NP doping with Tb^{3+} and Eu^{3+} ions, Gd^{3+} ions were introduced into hafnia NPs (10%) via sol-gel method, as gadolinium is

magnetic resonance imaging (MRI) active, and with this may render hafnia useful for combined CT and MRI imaging. Also gadolinium oxide NPs were synthesized via the sol-gel method to compare size and toxicity of Gd doped hafnia with its pure oxide Gd_2O_3. XRD patterns are shown in the supplemental information section in figure 1. Both Gd NPs show a cubic structure and a crystallite size of 6(2) nm. It can be affirmed that analogous to the trivalent Tb and Eu doping, 10% Gd introduction into hafnia stabilizes the cubic phase and reduces the crystallite size.

Method	Sample	Z-Average (nm)	STD (nm)	PdI	STD
Precipitation	uncalcined HfO_2	383.4	21.8	0.264	0.045
	HfO_2	353.7	10.9	0.288	0.009
	HfO_2:10%Tb	372.1	8.4	0.235	0.063
	HfO_2:10%Eu	543.9	28.0	0.287	0.047
Microwave	HfO_2	346.9	3.3	0.264	0.014
Sol-Gel	HfO_2	635.8	8.9	0.177	0.040
	HfO_2:10%Tb	696.5	11.2	0.187	0.035
	HfO_2:10%Eu	772.2	30.1	0.212	0.031
	HfO_2:10%Gd	680.2	7.0	0.137	0.042
	Gd_2O_3	510.9	4.3	0.242	0.034
Functionalized	PVP@HfO2	553.0	19.6	0.192	0.037
	APTES@HfO2	559.4	18.5	0.173	0.030

Table 4.3: Comparison of hydrodynamic sizes and PDI (polydispersity index) measured by DLS with standard deviation (STD).

DLS measurements showed hydrodynamic sizes of 410 ± 90 for precipitated, 700 ± 60 for sol-gel and 560 ± 10 for functionalized sol-gel hafnia-based nanoparticles on average. The detailed sizes are shown in table 4.3. Particles were all dispersed in water and prepared in a similar way. Therefore, the sizes give a good indication about the average agglomeration in water in comparison to each other. It is observable by eye, that the colloid when tip sonicated gets increasingly stable with sonication time. However, 10-20 min tip sonication at 70% amplitude is still not enough to make a stable colloid, which is reflected by the big hydrodynamic size compared to the crystallite size, and considering the high material density. The size deviation between sol-gel and precipitated samples could be attributed to a more dense and spherical agglomeration for the latter taking the TEM (figure 4.1) pictures

into account. Monodispersity and shape play a severe role in the quality of DLS measurements and its fitting process. Bigger agglomerated lumps scatter much more light than spherical monodisperse NPs and excessive scattering masks low intensity scattered light from smaller particles. Hence, broadened peaks emerge reducing confidence in the data. PDIs in the range between 0.1 and 0.4 are moderately polydisperse [8]. Despite the higher hydrodynamic size, the PDI is reduced in the sol-gel samples. To get a better colloid stability surfactants are generally used [8]. Here, functionalization with PVP or APTES increased dispersability (less sonication needed for dispersion) and decreased the hydrodynamic size, but the PDI remains high. Other techniques are needed to prove that functionalization was successful. More detailed insights about the actual sizes of agglomerations in polydisperse samples can be given by the more effective nanoparticle tracking analysis (Nanosight), and indeed it suggested, that there are also particles in the smaller regime (40 - 400 nm) present.

4.4 Functionalization of hafnium dioxide nanoparticles

As a next step, primary and secondary surface functionalization have been investigated. PVP was used because it can serve as dispersant and is a biocompatible polymer [25], while APTES was used as primary anchor for further functionalization with folic acid to allow for folate-receptor targeting [42].

Figure 4.5 shows a surface charge of about -45.6 ± 2.6 mV for unfunctionalized HfO$_2$ NPs. 10% doping decreases the surface charge by roughly 4, 6 and 8 mV for Tb, Gd and Eu ions, respectively. Gadolinium oxide NPs have a much lower surface charge (-22.4 ± 1.2 mV) at neutral pH. APTES and PVP functionalized NPs have surface charges of -21.6 ± 0.9 and -7.3 ± 0.6 mV, respectively. A change in surface charge can give hints towards whether functionalization was successful or not. For example in [41] silica NPs with surface potential of almost -40 mV owing to their surface silanol groups (Si–OH) were amino-functionalized to have a zeta potential of +10 to 20 mV at neutral pH. Here, PVP- and APTES- functionalization show a drastic reduction in surface charge which, however, is still negative. A successful
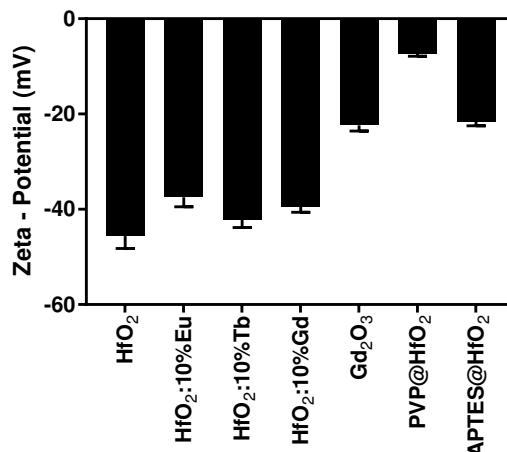
Figure 4.5: Comparison of surface charges in undoped, doped and surface functionalized HfO_2 nanoparticles. Sol-gel synthesized Gd_2O_3 NPs are also shown for comparison.

surface modification can, therefore, be suggested, but the extent of the modification is not fully clear.

IR-vibration spectroscopy reveals the groups which are present on the surface of the nanoparticles. PVP- and APTES-functionalized NPs show the presence of organic groups, and their spectra are compared to HfO_2 NPs (4.6). Especially the carbonyl stretching observed at 1650 cm^{-1} for PVP and the silane and amine stretchings around 980, 1600 and 3310 cm^{-1} and the CH_2 around 2920 cm^{-1} for APTES are very prominent absorption bands. All NPs show characteristic peaks for hafnium dioxide in the 'Reststrahlenband' from 500 to 800 cm^{-1}, which are not shown here and which even expands to $\sim$ 130 cm^{-1} [15].

In order to explore further bio-functionalization, APTES moieties were coupled to folic acid (FA). Folic acid could be used to selectively target folic acid positive tumor cells. Folate receptors have been shown to be highly overexpressed on the surface of many tumor types [57]. Intensity images from a microplate reader confirmed the presence of a green or red fluorescent secondary antibody on FA-functionalized NPs (figure 4.7). The corresponding collected light intensity ratios of particles functionalized with (figure 4.7 B (right)) versus without FA (figure 4.7
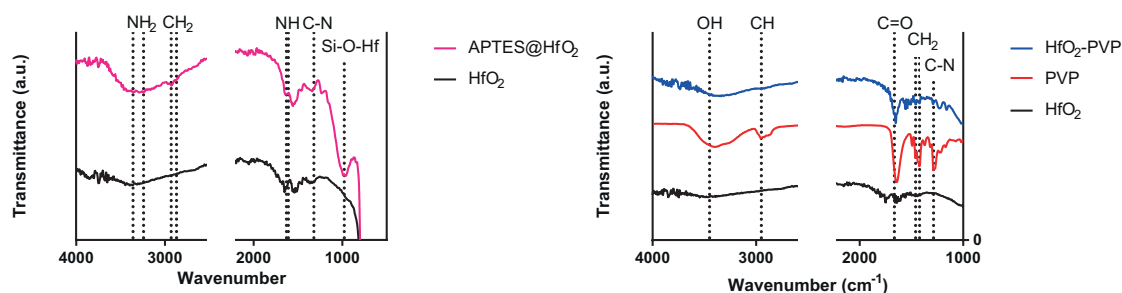
Figure 4.6: IR-absorption bands observed for APTES- (left) and PVP-functionalized (right) compared to the unfunctionalized HfO_2 NPs. Also shown is the IR-absorption of PVP alone.

B (left)) were 1.11, 1.18 and 1.34 for one, two and three drops of 5 µL particle suspension (1 mg/mL), respectively. This corresponds to 33 and 54% of the maximum light intensity measured at 15 µL, suggesting a linear dose response. These membranes have an amount of 33 and 66% of the maximum amount of FA-functionalized particles at 15 µL. Next to primary functionalization, also secondary functionalization has been successful. These results confirm that folic acid has been successfully coupled to the hafnia nanoparticles. Furthermore, the dot blot assay demonstrates that the folic acid is available for binding and hence such particles could in a next step be tested in an assay comparing the uptake in folic acid negative and positive cells.

4.5 Cyto- and hemocompatibility of hafnium dioxide nanoparticles

Cyto and hemocompatibility are imperative for the intravascular application of hafnia based probes. Therefore, first toxicity tests were carried out using an lactate dehydrogenase (LDH) release assay. This assay has been shown to be comparatively sensitive for the assessment of acute toxicity, and in particular the membrane damage potential of nanoparticles. To assess cytotoxicity of hafnia based NPs, LDH release from THP-1 and Caco-2 cells was measured and the results are shown in figure 4.8. Their cytotoxicity was compared to silica, which is used in drug delivery systems and gadolinium dioxide, commonly used as contrast agent.
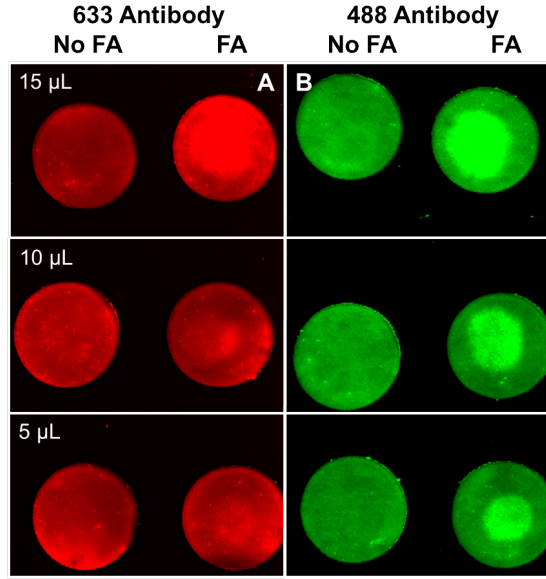
Figure 4.7: Fluorescence images of dot blot experiment using red (633) and green fluorescent (488) secondary antibody. Membranes are spotted with 3 different amounts of particle suspension either functionalized with folic acid (FA) or without (No FA).

Silica is known to cause LDH release [5] and to activate blood coagulation [20].

All NPs show a positive dose response, meaning higher LDH activity with higher dose, apart from silica NPs in THP-1 cells, which show a constant and very high level for all doses. In fact, it is around 70% compared to the positive control (PC), which is 0.1%TritonX-100, indicating a very high toxicity, such that no LDH increase is possible with increasing dose. All other NPs show LDH releases below 20% for THP-1 cells. In Caco-2 cells, only Gd_2O_3 shows no increase of toxicity for the highest two doses, which is hard to explain, since the first two doses induce LDH releases being amongst the highest, together with Tb- and Gd-doped HfO_2. However, assay interference can not be excluded and needs to be further investigated. A clear trend in Caco-2 cells can be observed. Undoped and Eu-doped HfO_2 together with silica NPs show the lowest and comparable toxicities (mean below 36% for all doses compared to PC). Tb and Gd doping seems to increase toxicity, with a mean up to 37 and 43% compared to PC for the highest dose, respectively. A possible cause to the increased LDH release might be ion release.
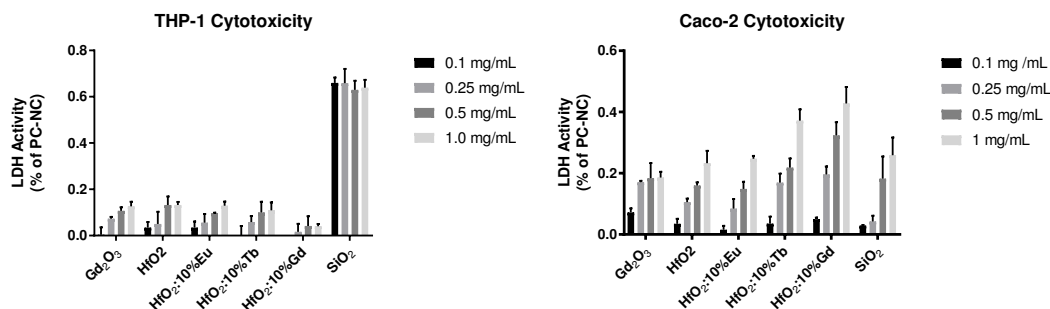
Figure 4.8: LDH release in THP-1 (left) and Caco-2 (right) cells for doped and undoped hafnium dioxide NPs in comparison to as synthesized sol-gel gadolinium oxide and pyrogenic(?) silica NPs, normalized to negative (NC=0) and positive control (PC=1).

Especially free Gd ions are considered harmful [40] which would explain the higher toxicity in our Gd-related NPs.

To determine ion leaching from the matrix, an elemental analysis was done for 10% doped Gd and Tb hafnia NPs which were dispersed at 1 mg/mL in citrate buffer at lysosomal pH (pH 4.5). Results in figure 4.9 reveal that after 1 day of incubation at 37 d°C, 4 - 6 µg/mL of Tb and Gd ions leached into the medium, which corresponds to 4 - 6 % of the expected total amount. Hafnium ions leached out only to an amount of 0.1% of the total expected amount. The higher amount of free Gd ions compared to Tb ions confirm the findings in higher toxicity for Caco-2 cells. Interestingly, the Gd ion leaching from hafnia can also be compared to Gd-oxide NPs (figure 4.9). Compared to the pure phase which dissolved almost completely in citrate buffer at lysosomal pH, hafnia is much more stable and Gd ions stay incorporated to a good extend (leaching up to 6% after 1 day). A subsequent more extensive ion release study for the NPs is already in progress to determine the leaching of dopant ions from the hafnia host matrix and to compare it in the case of gadolinium to the pure phase (Gd_2O_3) for different media and for longer incubation time.

However, the toxicity trend cannot be confirmed in the other cell line, THP-1, suggesting that different cell lines react differently to metal ions or NPs. Here all
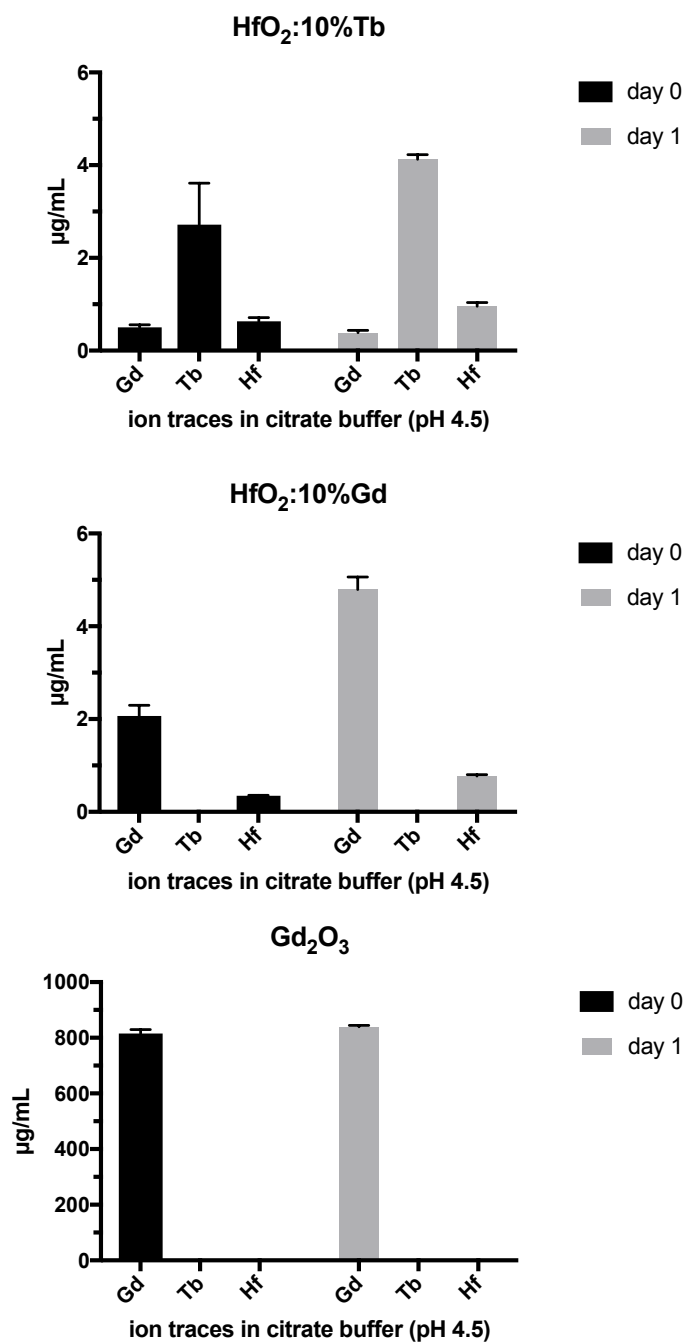
Figure 4.9: Elemental analysis (ICP-OES) of Tb, Gd and Hf ions for Tb and Gd doped hafnia nanoparticles and for gadolinium oxide NPs, which were suspended using tip sonication at 1mg/mL in citrate buffer at lysosomal pH 4.5. Analysis was done after suspension and after 1 day incubation at 37°C.

NPs show similar, low toxicity, with Gd-doped HfO_2 being the least toxic NPs. The most obvious difference in the cell lines is, that one is a adherent (Caco-2) and the other one a suspension culture. Thus the cell uptake of NPs might be different, especially if the NPs are not stable in medium and sediment quickly towards the bottom. This would explain the low toxicity in all NPs in the THP-1 line compared to the more stable silica NPs (as observed by eye after tip sonication), since the agglomerated HfO_2 and Gd_2O_3 (size around 700 nm) sedimented to the bottom of the well, whereas the SiO_2 NPs were easily taken up. Caco-2 cells adhere to the bottom favouring an uptake of the sedimented NPs, making silica appear less toxic especially compared to the other cell line. Either way, the dose response proves that there is a cytotoxic interaction of the NPs with the cells, regardless of cell type. Within the cell line, NPs with similar size and stability can be easily compared. Importantly, the nanoparticle doses investigated here are very high and assay interference needs to be investigated in more detail. Further studies, also using complementary assays, such as AnnexinV/PI and MTS assays are under way. Additionally, dosimetry calculations will be performed using a model established at Empa to correct for different sedimentation behaviours.

In terms of hemocompatibility, hemolysis and coagulation are the two most important parameters, along with the activation of the complement. Plasma coagulation and hemolysis activity of HfO_2, HfO_2:10%Tb and PVP-functionalized NPs was also assessed and are shown in figure 4.10. No effect on hemolysis, i.e. blood damage, was observed in the NPs compared to PC and fumed silica (A200). Particles led to a more pronounced plasma coagulation activation compared to negative control. While in the negative control a slow, near-linear increase of plasma coagulation is observed, the coagulation saturation for HfO_2 and HfO_2:10%Tb is already reached after 15 min, which is about 5 min later than saturation for the fumed silica A200 nanoparticles used for comparison. To that a striking difference was observed for PVP-functionalized NPs which show a similar, but steeper near-linear increase in coagulation than NC. Thus PVP surface modification markedly reduced plasma coagulation compared to bare NPs reducing the possible risk of thrombogenicity. It reflects a necessary step addressing safety concerns when NPs are interacting with the blood coagulation system.
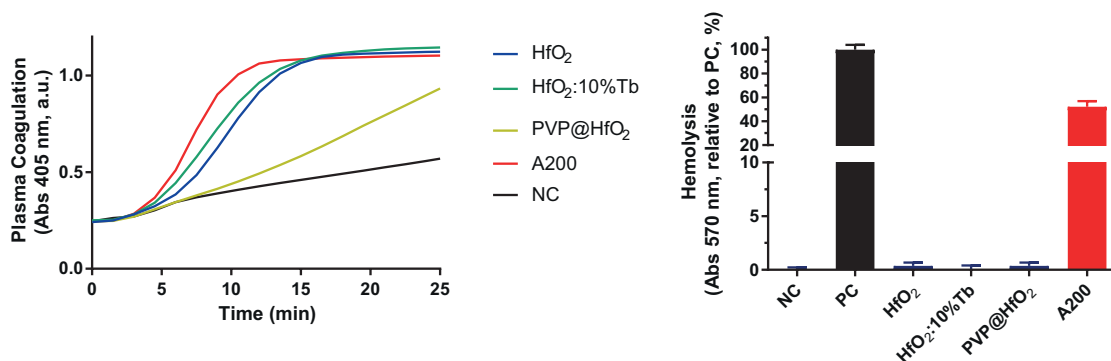
Figure 4.10: Coagulation (left) and hemolysis (right) activity for undoped, Tb-doped and PVP-functionalized HfO$_2$ NPs in comparison to fumed silica A200 NPs, negative (NC) and positive control (PC).

4.6 Radioenhancement effects of hafnium dioxide nanoparticles

In order to explore the radio-sensitization effect of the synthesized hafnia NPs, X-ray irradiation experiments were performed. Cells and cells with supplemented NPs were exposed to different radiation doses and cell viability was compared to non-irradiated cells.

Figure 4.11 shows the results of the cell MTS assay and the FACS analysis of PI-stained cells after irradiation with 0, 1, 2, 6 or 12 Gy. MTS was done 5 days after irradiation, and shows that with increasing radiation dose the cell viability decreases for all conditions. The addition of particles seems to have a small, but minor effect on cell viability with no radiation treatment (0 Gy) and with a dose treatment of 1 Gy. At 2 and 6 Gy dose treatment, the difference in cell viability between conditions are most prominent, with highest viability for cells without NPs, and lowest viability for 10% Tb-doped HfO$_2$. At 12 Gy all cell conditions are on a similar low viability level of around 40%. Exemplarily, gated FACS measurements of PI-stained cells for 0 and 2 Gy irradiation concord well with the MTS assay findings. 2 Gy is a dose fractionation widely used in clinical practice for curative treatments [39]. Therefore, it can make sense to evaluate the survival fraction at 2 Gy and compare them between conditions to give the nanoparticle-mediated

enhancement ratio (NER) and assess radioenhancement by NPs. The NER is a special case of the dose modifying factor (DMF) which is based on survival curves fitted by the linear-quadratic model [39]. In principle the NER is the ratio of the viability of cells together with NPs vs. the viability of control cells at the same dose value. Here, we can report the NER for 2 and 6 Gy which are different from 1. These are 0.75 ± 0.14 and (HfO$_2$ NPs) and 0.75 ± 0.08 (HfO$_2$:10%Tb NPs) for NER2 and 0.84 ± 0.19 (HfO$_2$ NPs) and and 0.71 ± 0.20 (HfO$_2$:10%Tb NPs) for NER6 based on MTS assay. The error is based on standard deviations and Gaussian uncertainty propagation. Though clonogenic assays, taking into account the 'cell reproductive death', are the gold standard for in vitro evaluation of the cytotoxicity of ionizing radiations, several studies have shown that results of metabolic assays and clonogenic assays can be concordant [39]. The MTS time point of 5 days after irradiation was chosen in order to allow irradiated cells to regain exponential growth. Measuring MTS too early would lead to an overestimation of cell viability because cells are still in the growth lag phase [35]. This might explain the not observed radiosensitization effect for the greatest dose (12 Gy), for which the time point of MTS assay would have to be adapted to a later day.
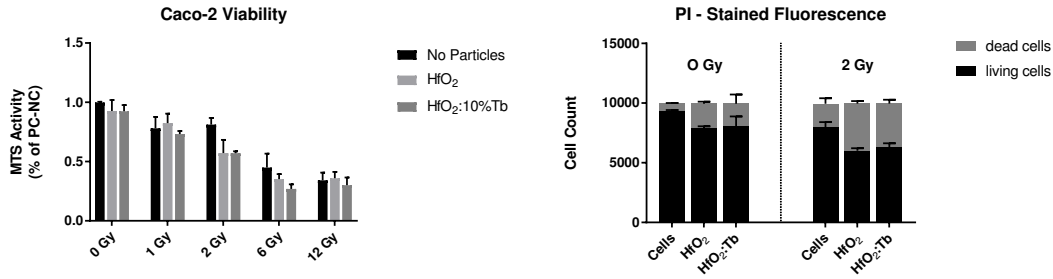
Figure 4.11: Caco-2 cell viability after irradiation of cells with different doses evaluated by MTS assay (A) and FACS measurement using PI staining (B). Viability of cells with no particles, undoped and 10% Tb-doped HfO$_2$ NPs are compared. PC: positive control (TritonX-100); NC: negative control (cells without radiation treatment)

CHAPTER 5

Conclusion

This work demonstrates the versatile potential of hafnium dioxide as a host matrix for multimodal theranostic imaging probes.

First, in a comparative study it was demonstrated that the sol-gel method (according to [37], is superior to precipitation (according to [36] or microwave-assisted precipitation in terms of particle size distribution and dopand ion incorporation efficiency. Second, it was shown that hafnia can be surface-functionalized with cytocompatible polymers and primary anchors using simple one-pot protocols. APTES moieties can then be used as a platform for further bio-functionalization as such as folic acid (FA). In this regard the availability of FA to a FA-antibody was demonstrated in a dot blot assay. Third, it was shown how hemocompatibility can be modulated by surface chemistry and preliminary cytocompatibility results show relatively good compatibility even at high concentrations. In fact, the hafnia reduces ion leaching from the host matrix for dopands such as Gd^{3+} compared to the pure phase (Gd_2O_3), as evidenced by ICP measurements on the ion release from the hafnia matrix over time. Finally, the promise for hafnia as radiosensitizer was displayed.

While more detailed investigations on compatibility and therapeutic efficacy are needed, the present study illustrates manifold properties of hafnia-based nanomaterials beyond radio-enhancing and the potential of hafnia as a new generation

multimodal theranostic agent. This work will be continued in a follow up-study to reveal if toxic ion leaching can be prevented by a stable incorporation of trivalent ions into hafnia and to investigate the efficacy of REE-doped hafnia nanoparticles in different in vitro and in vivo settings, including X-ray and Protontherapy.

Supplemental Information
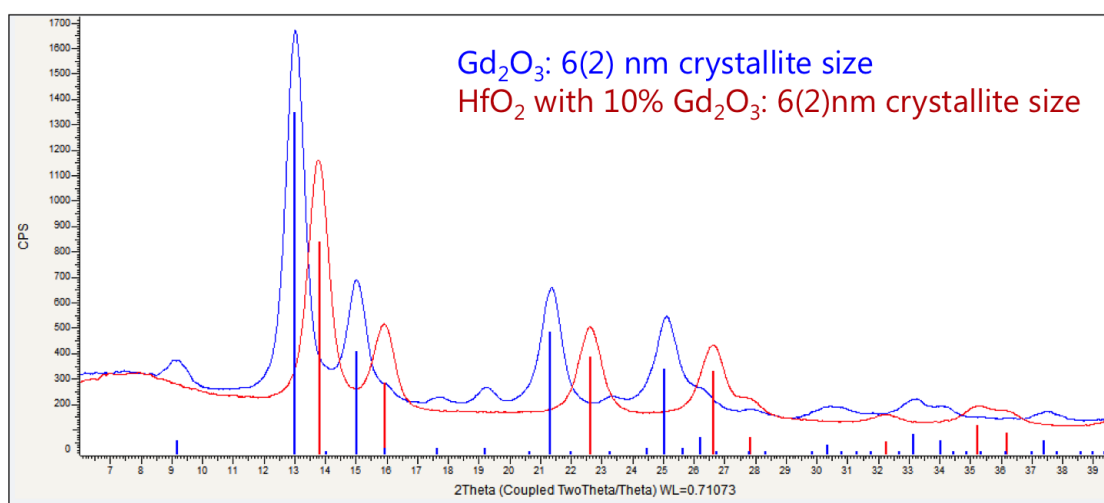
Figure 1: Superposition of raw XRD data with reference peaks from xrd-database for cubic Gd_2O_3 with space group (Ia-3) and cubic HfO_2 with space group (Fm-3m).

List of Figures

46

List of Tables

Bibliography

[1] D. M. Adams, S. Leonard, D. R. Russell, and R. J. Cernik. X-ray diffraction study of hafnia under high pressure using synchrotron radiation. *Journal of Physics and Chemistry of Solids*, 52(9):1181–1186, 1991.

[2] M. W. Ahmad, W. Xu, S. J. Kim, J. S. Baeck, Y. Chang, J. E. Bae, K. S. Chae, J. A. Park, T. J. Kim, and G. H. Lee. Potential dual imaging nanoparticle: Gd2o3 nanoparticle. *Scientific reports*, 5:8549, 2015.

[3] C. S. Almeida, I. K. Herrmann, P. D. Howes, and M. M. Stevens. Tailoring cellular uptake of conjugated polymer nanoparticles using modular amphiphilic peptide capping ligands. *Chemistry of Materials*, 27(19):6879–6889, 2015.

[4] A. C. Anselmo and S. Mitragotri. Nanoparticles in the clinic. *Bioengineering & Translational Medicine*, 1(1):10–29, 2016.

[5] H. Bahadar, F. Maqbool, K. Niaz, and M. Abdollahi. Toxicity of nanoparticles and an overview of current experimental models. *Iranian biomedical journal*, 20(1):1–11, 2016.

[6] F. Benz and H. P. Strunk. Rare earth luminescence: A way to overcome concentration quenching. *AIP Advances*, 2(4):042115, 2012.

[7] E. Bersch, S. Rangan, R. A. Bartynski, E. Garfunkel, and E. Vescovo. Band offsets of ultrathin high-k oxide films with si. *Physical Review B*, 78(8):141, 2008.

[8] S. Bhattacharjee. Dls and zeta potential - what they are and what they are not? *Journal of controlled release : official journal of the Controlled Release Society*, 235:337–351, 2016.

[9] K. Binnemans. Interpretation of europium(iii) spectra. *Coordination Chemistry Reviews*, 295:1–45, 2015.

[10] D. Bobo, K. J. Robinson, J. Islam, K. J. Thurecht, and S. R. Corrie. Nanoparticle-based medicines: A review of fda-approved materials and clinical trials to date. *Pharmaceutical research*, 33(10):2373–2387, 2016.

[11] A. Boukerika and L. Guerbous. Annealing effects on structural and luminescence properties of red eu3+-doped y2o3 nanophosphors prepared by sol–gel method. *Journal of Luminescence*, 145:148–153, 2014.

[12] K. T. Butterworth, S. J. McMahon, F. J. Currell, and K. M. Prise. Physical basis and biological mechanisms of gold nanoparticle radiosensitization. *Nanoscale*, 4(16):4830–4838, 2012.

[13] Y. W. Chen, M. Liu, T. Kaneko, and P. C. McIntyre. Atomic layer deposited hafnium oxide gate dielectrics for charge-based biosensors. *Electrochemical and Solid-State Letters*, 13(3):G29, 2010.

[14] J. de Roo, I. van Driessche, J. C. Martins, and Z. Hens. Colloidal metal oxide nanocrystal catalysis by sustained chemically driven ligand displacement. *Nature materials*, 15(5):517–521, 2016.

[15] O. Dominguez, T. L. McGinnity, R. K. Roeder, and A. J. Hoffman. Mid- and far-infrared optical characterization of monoclinic hfo 2 nanoparticles and evidence of localized surface phonon polaritons. SPIE Proceedings, page 101001G. SPIE, 2017.

[16] M. L. Etheridge, S. A. Campbell, A. G. Erdman, C. L. Haynes, S. M. Wolf, and J. McCullough. The big picture on nanomedicine: the state of investigational and approved nanomedicine products. *Nanomedicine : nanotechnology, biology, and medicine*, 9(1):1–14, 2013.

[17] J. A. Field, A. Luna-Velasco, S. A. Boitano, F. Shadman, B. D. Ratner, C. Barnes, and R. Sierra-Alvarez. Cytotoxicity and physicochemical properties of hafnium oxide nanoparticles. *Chemosphere*, 84(10):1401–1407, 2011.

[18] S. Gálvez-Barboza, L. A. González, B. A. Puente-Urbina, E. M. Saucedo-Salazar, and L. A. García-Cerda. Preparation and characterization of ce-doped hfo2 nanoparticles. *Journal of Alloys and Compounds*, 643:S62–S66, 2015.

[19] T. Gayathri, N. M. Sundaram, and R. A. Kumar. Gadolinium oxide nanoparticles for magnetic resonance imaging and cancer theranostics. *Journal of Bionanoscience*, 9(6):409–423, 2015.

[20] A. N. Ilinskaya and M. A. Dobrovolskaia. Nanoparticles and the blood coagulation system. part ii: Safety concerns. *Nanomedicine (London, England)*, 8(6):969–981, 2013.

[21] V. Jayaraman, G. Bhavesh, S. Chinnathambi, S. Ganesan, and P. Aruna. Synthesis and characterization of hafnium oxide nanoparticles for bio-safety. *Materials Express*, 4(5):375–383, 2014.

[22] C. Jiang, F. Wang, N. Wu, and X. Liu. Up- and down-conversion cubic zirconia and hafnia nanobelts. *Advanced Materials*, 20(24):4826–4829, 2008.

[23] A. A. Khorasani, J. L. Weaver, and C. Salvador-Morales. Closing the gap: Accelerating the translational process in nanomedicine by proposing standardized characterization techniques. *International Journal of Nanomedicine*, 9:5729–5751, 2014.

[24] D.-J. Kim, S.-H. Hyun, S.-G. Kim, and M. Yashima. Effective ionic radius of y3+ determined from lattice parameters of fluorite-type hfo2 and zro2 solid solutions. *Journal of the American Ceramic Society*, 77(2):597–599, 1994.

[25] K. M. Koczkur, S. Mourdikoudis, L. Polavarapu, and S. E. Skrabalak. Polyvinylpyrrolidone (pvp) in nanoparticle synthesis. *Dalton transactions (Cambridge, England : 2003)*, 44(41):17883–17905, 2015.

[26] S. Lange, V. Kiisk, J. Aarik, M. Kirm, and I. Sildos. Luminescence of zro2 and hfo2 thin films implanted with eu and er ions. *physica status solidi (c)*, 4(3):938–941, 2007.

[27] A. Lauria, I. Villa, M. Fasoli, M. Niederberger, and A. Vedda. Multifunctional role of rare earth doping in optical materials: Nonaqueous sol-gel synthesis of stabilized cubic hfo2 luminescent nanoparticles. *ACS nano*, 7(8):7041–7052, 2013.

[28] F. Lux, L. Sancey, A. Bianchi, Y. Crémillieux, S. Roux, and O. Tillement. Gadolinium-based nanoparticles for theranostic mri-radiosensitization. *Nanomedicine (London, England)*, 10(11):1801–1815, 2015.

[29] M. T. Matter, F. Starsich, M. Galli, M. Hilber, A. A. Schlegel, S. Bertazzo, S. E. Pratsinis, and I. K. Herrmann. Developing a tissue glue by engineering the adhesive and hemostatic properties of metal oxide nanoparticles. *Nanoscale*, 9(24):8418–8426, 2017.

[30] Y. Min, J. M. Caster, M. J. Eblan, and A. Z. Wang. Clinical translation of nanomedicine. *Chemical reviews*, 115(19):11147–11190, 2015.

[31] E. Montes, P. Cerón, T. Rivera Montalvo, J. Guzmán, M. García-Hipólito, A. B. Soto-Guzmán, R. García-Salcedo, and C. Falcony. Thermoluminescent characterization of hfo2:tb3+ synthesized by hydrothermal route. *Applied*

radiation and isotopes : including data, instrumentation and methods for use in agriculture, industry and medicine, 83 Pt C:196–199, 2014.

[32] H. B. Na, I. C. Song, and T. Hyeon. Inorganic nanoparticles for mri contrast agents. *Advanced Materials*, 21(21):2133–2148, 2009.

[33] M. N. Polyanskiy. Refractive index database. `https://refractiveindex.info`. Accessed on 2017-09-04.

[34] A. Pottier, E. Borghi, and L. Levy. New use of metals as nanosized radioenhancers. *Anticancer research*, 34(1):443–453, 2014.

[35] P. Price and T. J. McMillan. Use of the tetrazolium assay in measuring the response of human tumor cells to ionizing radiation. *Cancer research*, 50(5):1392–1396, 1990.

[36] A. Ramadoss, K. Krishnamoorthy, and S. J. Kim. Novel synthesis of hafnium oxide nanoparticles by precipitation method and its characterization. *Materials Research Bulletin*, 47(9):2680–2684, 2012.

[37] R. Ramos-González, L. A. García-Cerda, H. N. Alshareef, B. E. Gnade, and M. A. Quevedo-López. Study of hafnium (iv) oxide nanoparticles synthesized by polymerized complex and polymer precursor derived sol-gel methods. *Materials Science Forum*, 644:75–78, 2010.

[38] P. Rauwel, E. Rauwel, C. Persson, M. F. Sunding, and A. Galeckas. One step synthesis of pure cubic and monoclinic hfo 2 nanoparticles: Correlating the structure to the electronic properties of the two polymorphs. *Journal of Applied Physics*, 112(10):104107, 2012.

[39] P. Retif, S. Pinel, M. Toussaint, C. Frochot, R. Chouikrat, T. Bastogne, and M. Barberi-Heyob. Nanoparticles for radiation therapy enhancement: The key parameters. *Theranostics*, 5(9):1030–1044, 2015.

[40] K. T. Rim, K. H. Koo, and J. S. Park. Toxicological evaluations of rare earths and their health impacts to workers: A literature review. *Safety and health at work*, 4(1):12–26, 2013.

[41] J. Samuel, O. Raccurt, O. Poncelet, A. Auger, W.-L. Ling, P. Cherns, D. Grunwald, and O. Tillement. Surface characterizations of fluorescent-functionalized silica nanoparticles: From the macroscale to the nanoscale. *Journal of Nanoparticle Research*, 12(6):2255–2265, 2010.

[42] E. I. Sega and P. S. Low. Tumor detection using folate receptor-targeted imaging agents. *Cancer and Metastasis Reviews*, 27(4):655, Jun 2008.

54

[43] J. R. Silva, A. S. Gouveia-Neto, and L. A. Bueno. Multicolor frequency upconversion luminescence in europium/terbium co-doped ytterbium-sensitized fluorogermanate glass excited at 980 nm. SPIE Proceedings, page 89641A. SPIE, 2014.

[44] S. Svenson. Clinical translation of nanomedicines. *Current Opinion in Solid State and Materials Science*, 16(6):287–294, 2012.

[45] Tracie L. McGinnity, Owen Dominguez, Tyler E. Curtis, Prakash D. Nallathamby, Anthony J. Hoffman, Ryan K. Roeder. Hafnia (hfo2) nanoparticles as an x-ray contrast agent and mid-infrared biosensor.

[46] J. Venkatachalam, S. Ganesan, and P. Aruna. Synthesis and characterization of europium doped hafnium oxide nanoparticles by precipitation method. 8:1131–1138, 2015.

[47] J. Vuojola and T. Soukka. Luminescent lanthanide reporters: New concepts for use in bioanalytical applications. *Methods and Applications in Fluorescence*, 2(1):012001, 2014.

[48] N. Wan, J. Xu, T. Lin, X. Zhang, and L. Xu. Energy transfer and enhanced luminescence in metal oxide nanoparticle and rare earth codoped silica. *Applied Physics Letters*, 92(20):201109, 2008.

[49] L. Wang, X. Xue, F. Shi, D. Zhao, D. Zhang, K. Zheng, G. Wang, C. He, R. Kim, and W. Qin. Ultraviolet and violet upconversion fluorescence of europium (iii) doped in yf(3) nanocrystals. *Optics letters*, 34(18):2781–2783, 2009.

[50] S. Wilhelm, A. J. Tavares, Q. Dai, S. Ohta, J. Audet, H. F. Dvorak, and W. C. Chan. Analysis of nanoparticle delivery to tumours. *Nature Reviews Materials*, 1:16014, 2016.

[51] G. D. Wilk, R. M. Wallace, and J. M. Anthony. High-k gate dielectrics: Current status and materials properties considerations. *Journal of Applied Physics*, 89(10):5243–5275, 2001.

[52] Y. Xu, M. Yamazaki, and P. Villars. Inorganic materials database for exploring the nature of material. *Japanese Journal of Applied Physics*, 50(11):11RH02, 2011.

[53] L. Yu and M. Nogami. Up-conversion luminescence of terbium(iii) in sio 2 and zno–sio 2 glasses induced by simultaneous absorption of three photons and saturation. *Spectroscopy Letters*, 41(7):344–348, 2008.

[54] L. Yu and M. Nogami. Upconversion luminescence properties of europium in zno–sio2 glasses by femtosecond laser excitation. *Materials Chemistry and Physics*, 107(2-3):186–188, 2008.

[55] L. Zhang, R. Yang, H. Zou, X. Shen, J. Zheng, and W. Wei. High-efficiency simultaneous three-photon absorption upconversion luminescence of a terbium-doped germanate glass. *Japanese Journal of Applied Physics*, 55(12):122402, 2016.

[56] X. Zhao and D. Vanderbilt. First-principles study of structural, vibrational, and lattice dielectric properties of hafnium oxide. *Physical Review B*, 65(23):126, 2002.

[57] G. L. Zwicke, G. A. Mansoori, and C. J. Jeffery. Utilizing the folate receptor for active targeting of cancer nanotherapeutics. *Nano Reviews*, 3(1):18496, 2012.